Colloids and Surfaces A: Physicochemical and Engineering Aspects

https://www.sciencedirect.com/journal/colloids-and-surfaces-a-physicochemical-and-engineering-aspects

Impact factor: 4.539

Accepted January 25th 2022

COMPUTATION OF MAGNETOHYDRODYNAMIC ELECTRO-OSMOTIC MODULATED ROTATING SQUEEZING FLOW WITH ZETA POTENTIAL EFFECTS

[1]R. Balaji, [2]J. Prakash, [*3]Dharmendra Tripathi and [4]O. Anwar Bég

[1]Department of Mathematics, Panimalar Institute of Technology, Chennai - 600123, Tamil Nadu, India.
balaji_2410@yahoo.co.in

*[2]Department of Mathematics, Avvaiyar Government College for Women, Karaikal – 609 602, Puducherry-U.T., **India.** prakashjayavel@yahoo.co.in*

*[3]Department of Mathematics, National Institute of Technology Uttarakhand, Srinagar– 246174, **India.** dtripathi@nituk.ac.in*

*[4]Multi-Physical Engineering Sciences Group, Dept. Mechanical and Aeronautical Engineering, SEE, Salford University, Manchester, M54WT, **UK**. gortoab@gmail.com*

***Corresponding author: dtripathi@nituk.ac.in** (D. Tripathi)*

ABSTRACT

Motivated by exploring novel intelligent functional materials deployed in electromagnetic squeezing flows such systems, a comprehensive mathematical model is developed to investigate the squeezing flow of a smart viscous ionic magneto-tribological fluid with zeta potential effects, intercalated between two parallel plates rotating in unison, under the simultaneous application of electric and magnetic fields. The lower disk permits lateral mass flux (suction or injection). Continuity and momentum equations are represented in the proposed three-dimensional mathematical model by a set of partial differential equations. The electro-viscous effects resulting from distorted electric double-capacity flow fields are comprehensively examined for various intensities of applied plate motion. The formulation features a more robust approach to the traditional Poisson-Boltzmann equation model. A similarity transformation is used to translate the governing equations into ordinary differential equations, which are then numerically solved with appropriate boundary conditions at the disks using MATLAB software. Via graphical visualization of velocity profiles, pressure gradients and the upper wall coefficient of skin friction, several characteristics of squeezing flow are analysed. The computations show that there is a rise in pressure near the plate walls and a fall in pressure in the centre with increment in rotational, electroosmosis, electric field, and magnetic parameters. However, by selecting the appropriate squeezing velocity, the viscous drag on the lower plate can be effectively reduced. It is also observed that as the disk (wall) suction parameter increases, both radial and transverse velocities are damped. The current study generalizes previous investigations with the novelty of rotation and also pressure gradient computations. Furthermore, it provides a useful benchmark for alternative numerical simulations.

KEYWORDS: *Squeezing flow; Rotation; HPM; Zeta potential; Electro-osmosis; Magnetic field.*

1. INTRODUCTION

Squeezing flow is fundamental to the operation of numerous bearing systems in modern engineering tribology [1]. It features in polymer mould injection, gas turbine systems, locomotive bearings, composite materials synthesis, rheometry, synovial biomechanics and food processing. Approaching surfaces in squeezing flows often feature parallel disks which generate compression in the intercalating fluid via an external applied stress. Traditionally studies of squeezing flows have employed the classical Reynolds lubrication equation. However, in situations featuring complex boundary conditions, unsteady effects, inertia, sophisticated lubricants, rough geometries, slip effects and supplementary body forces, a more comprehensive approach is required. The Reynolds equation, while useful for estimating pressure distribution and film thickness, is not adequate for providing a comprehensive picture of the intricate momentum characteristics in such regimes [2-4]. The Navier-Stokes partial differential equations however can often be reduced to much simpler ordinary differential equation systems via similarity transformations to simulate more elegant squeezing flow problems. In recent years many investigations have been conducted examining complex squeezing flows with this approach and exploring other phenomena such as heat and mass diffusion and multi-physical/chemical effects. The squeezed dynamics analysis for heat transmission on a porous surface was reported by Mahmood *et al.* [5]. Hayat *et al*. [6] considered the effects of chemical reactions and heat conductivity on squeezing motion.

Additionally, the introduction of ionic and magnetic lubricants has mobilized new work in magnetohydrodynamic and electrokinetic squeezing flows. Ionic lubrication [7] features electro-kinetic flows which arise when a peripheral electric field is applied between the inlet and outlet of a channel. The ionic (polar) fluid develops near-wall layers of counter-ions within the fluid, resulting mobilizing flow of the electrolyte through the system. In contrast, the neutral core gets seized by the electric field and moves like a solid object [8]. In an experiment with porous clay in 1809, Reuss [9] proved the concept of electrokinetic flow for the first time. Magnetohydrodynamics (MHD) involves the interaction of external static or oscillating magnetic fields with viscous fluids. Magnetic lubrication therefore deploys electrically conducting fluids which respond to an external magnetic field [10]. MHD also features in many other applications in biomedical systems including blood flows [11-13]. Many theoretical and numerical studies of both electro-osmotic lubrication and hydromagnetic lubrication have been conducted including squeezing flows. Li and Jin [14] developed a tribological model including the coupled effects of electric double layer (EDL) and boundary slip. Using the Debye—Hückel

approximation for low surface potential and the Navier-Stokes equation with body force due to the electrical potential with Navier slip boundary conditions, they derived expressions for velocity distributions, apparent viscosity and the modified Reynolds lubrication equation, showing that load capacity is enhanced with a reduction in inverse Debye length and slip lengths and with increment in electro-viscosity. Further studies include Phillips and Zabinski [15] (on ceramic electro-kinetic lubrication) and Wong *et al.* [16] (on electric double layer effects in slender aqueous films). Talapatra and Chakraborty [17] investigated the squeezing flow between two charged parallel plates with electric double layer overlap effects. They showed that the classical Poisson-Boltzmann equation may be inaccurate for squeezing flow in very narrow regimes where instantaneous liquid layer thickness is the same or thinner than the characteristic electric double layer thickness, for which there exists a deficit of counterions within the bulk liquid owing to a surplus in the electrical double layer or vice versa. Zhao *et al.* [18] *investigated the squeezing flow between* charged curved and a flat surface as a model of the tip–substrate configuration in electrolytic dynamic atomic force microscopy. They utilized the Derjaguin–Landau–Verwey–Overbeek theory, noting that the electro-viscous effect strongly increases the dissipative hydrodynamic interaction force and sharpens the velocity profiles in the thin electrolyte solution film. Magnetofluid squeeze film studies Noor *et al*. [19] who examined transient viscoelastic radiative reactive squeezing flow between two plates using a finite difference procedure. Shah and Patel [20] deployed the Rosensweig ferrohydrodynamic theory to derive a general modified Reynolds equation for ferrofluid (FF) lubricated circular discs porous squeeze film-bearings, under oblique and radially variable magnetic field. They considered several different circular porous squeeze film-bearing configurations including the exponential, secant and parallel (flat)) designs. Domairry and Aziz [21] used a homotopy perturbation (HPM) to compute the MHD squeezing flow between parallel discs under axial static magnetic field. Adesanya *et al.* [22] used the Adomian decomposition method (ADM) and Runge-Kutta Shooting Method (RKSM) to simulate the time-dependent squeezing flow of a magnetic Eyring-Powell liquid between parallel plates with radiative flux and internal heat generation/absorption effects associated with exothermic or endothermic nature of the reaction. They showed that the flow is damped with reducing magnetic field (Hartmann number) for expanding walls (plates moving apart) whereas contraction (squeezing) of the channel walls, heat generation, and radiation parameters elevate the Nusselt number. Umavathi *et al.* [23] computed the transient squeezing magnetized nanofluid film flow with mixed thermal boundary conditions imposed at the plates. They observed that larger Hartmann number (i. e. stronger axial magnetic field) reduces velocity in the intermediate zone, and that nanoparticles reduce heat build-up in

squeezing films, which helps to prevent corrosion and plate internal surface deterioration. Prajapati [23] studied the hydromagnetic squeeze film between rough porous truncated conical plates under an oblique magnetic field and deployed a stochastic random roughness model for the bearing surfaces. They showed that there is a substantial boost in the pressure, load carrying capacity and response time with increment in magnetization parameter and that lubrication performance is also enhanced with negatively skewed roughness. Further studies include Khan *et al.* [25] who used the Variation of Parameters Method (VPM) to study MHD squeezing flow between two infinite plates, observing strong deceleration in the axial flow with increasing magnetic field and acceleration with increment in Reynolds number. In all of these investigations, magnetic lubricants have been shown to increase efficiency by controlling lubricant viscosity fluctuation under high operating conditions. It was also found that the *electro-viscous* impact on squeezing streams of thin electrolyte sheets limited between two curved and flat charged surfaces could be accounted for by employing lubrication assumptions. This approach involves the solution of the Nernst, Planck and Poisson/Navier–Stokes equations and enables the identification of how electro-viscous effects at a specific zeta potential is influenced by an EDL counterion conductivity, resulting in a much sharper velocity distribution.

Under the influence of an applied electric field, ions in aqueous ionic liquids are carried through the capillary wall by electroosmosis. For bio-microfluidic systems, there is a need to build mathematical models to describe in a more refined fashion the physiological transport process and construct optimized bio-microfluidic devices [8]. For different flow geometries, such as capillaries, channels and capillary annulus configurations, basic mathematical models for electroosmotic squeezing flows as described earlier have identified the importance also of *zeta potential* effects. Other studies have also confirmed this in biomicrofluidics [26-29]. For electrokinetically propelled movements, Helmholtz presented theoretical research on the electric double layer (EDL) in 1879 [30]. In the early 1900s, Von Smoluchowski [31] heavily influenced the understanding of electrokinetically propelled streams, particularly when the EDL thickness is significantly less than the channel height. It has further been identified that when the double layer is thin compared to the minimum distance separating charged surfaces e. g. in a squeezing plate system, the electro-kinetic force magnitude can be manipulated relative to viscous force [7]. Burgreen and Nakache [32] used the Debye–Hückel linear method to calculate the applied electric distribution to study the effect of surface potential on liquid flow via ultrafine slits. Very recently Prakash *et al.* [33] have generalized previous Newtonian studies to consider the impact

of electrical double layer (EDL) in bio-inspired propulsion of non-Newtonian PTT liquids in micro-channels.

Combined MHD and electro-osmotic transport has recently also emerged as novel hybrid approach for designing micro-fluidic systems and offers significant promise also in tribological engineering. Frequently an axial electrical field is used in conjunction with a transverse magnetic field to offer a dual mechanism for regulating ionic magnetic lubricant flows. Interesting studies in electro-magnetohydrodynamics (EMHD) include Bharathi *et al.* [34] who studied the combined effects of electrical and magnetic fields in electro-osmotic magnetized hybrid nanofluid flow from an exponentially accelerated wall with radiative heat flux. Prakash *et al.* [35] investigated the EMHD peristaltic pumping flow of a Williamson rheological liquid. They computed the influence of Debye-Hückel parameter, Helmholtz-Smoluchowski velocity, zeta potential and Hartmann number on pumping characteristics, shear stress and trapping patterns. Further studies include Rajaram *et al.* [36] who have shown the very different effects induced with axial electrical field direction and also transverse magnetic field strength on momentum and heat transfer characteristics in EMHD flows.

The above investigations have generally neglected rotational body force effects. However, in emerging lubrications systems e. g. electro-osmotic travelling wave bearings [37], *rotation* is critical. Other industrial and technical operations also feature rotating channel/plate/wall fluid dynamics. Further analyses of non-conducting rotating flows have been communicated by Turkyilmazoglu [38-39] and also magnetohydrodynamic rotating stretching disk flows [40, 41]. All these investigations confirmed the substantial modification in momentum and thermal characteristics with Coriolis body force effect and featured various parameters to simulate this effect including Rossby number and Ekman number. It is important to note that the measurement of mass flow rate is greatly dependent on the Coriolis force in spinning devices and equipment such as radial micro-pumps and rotating shock absorbers which feature squeezing flows. This has motivated interest in the rotational squeezing flows. Many studies have been communicated considering either non-conducting or electrically conducting fluid under the action of electrical field, magnetic field or both. Munawar *et al.* [42] simulated the squeezing flow of a magnetized liquid in a rotating parallel plate channel with a lower stretching porous wall. They observed that substantial pressure variation is induced close to the plate boundaries with magnetic field and that the downward motion of upper plate leads to acceleration in the forward flow and viscous drag on lower plate, whereas upward motion generates backflow. Arain *et al*. [43] used a combination of the differential transform method (DTM) and Padé approximants to simulate the squeezing

nanofluid magnetized flow between rotating circular plates doped with micro-organisms, as a model of bio-inspired nano-lubrication. Magnetic induction effects in rotating dual disk MHD squeezing flow were investigated by Zueco and Bég [44] using the PSPICE electrothermal software. Bég *et al.* [45] deployed an Adomian decomposition method (ADM) to compute the radial and tangential induced magnetic field and velocity field in squeezing rotating magnetic film lubrication between coaxial rotating disks with Batchelor number effects for a range of squeezing scenarios. Khatun *et al*. [46] utilized an explicit finite difference method to analyze the combined effects of electrical and magnetic fields on squeezing flow in a rotating electromagnetic sensor (Riga plate) regime with radiative flux. Riasat *et al.* [47] examined magnetic rotating nanofluid squeezing films with induction effects). Siva *et al*. [48] studied non-Newtonian magnetic electro-osmotic squeezing flow in a rotating microfluidic channel with thermal effects. Further investigations include Abhimanyu *et al.* [49] (on viscoelastic rotating electro-kinetic flow), Li *et al.* [50] (on third grade elastico-viscous rotating electro-osmotic microchannel flow), Qi *et al.* [51] (on spinning Eyring electro-kinetic flow) and Siva *et al*. [52] (on time-dependent aqueous ionic couple stress rotating electrokinetic flow). All these studies have confirmed the marked modifications in fluid characteristics achieved with electrical and magnetic fields in conjunction with rotational body forces.

To the best of the authors' knowledge, a scrutiny of the technical literature has shown that thus far zeta potential effects however have not been examined in combined rotating EMHD squeeze film flow between disks. This is the motivation of the present study. A mathematical model for coupled electro-magnetic-hydrodynamic viscous squeezing flow *with rotational body force* and zeta potential effects is therefore developed in the present article. The electro-osmotic MHD rotating squeezing flow model is rendered dimensionless and solved numerically, subject to appropriate boundary conditions, with MATLAB software [53]. Extensive visualization of momentum characteristics is included. Significant modifications in these characteristics are observed due to rotational, squeezing, magnetic and electrical body force effects. The simulations are relevant to hybrid electromagnetic lubrication in micro-tribological systems.

2. MATHEMATICAL MODEL FORMULATION

As shown in Figure 1, unsteady three-dimensional incompressible, viscous, squeezing flow between coaxial rotating parallel plates is investigated. The X-axis runs parallel to the plate planes, while the Y-axis is perpendicular to the plates in a Cartesian coordinate system (X, Y).

Ionic fluid electrical net charge thickness and other body forces are ignored when the suspended particles move in front of a magnetic field, $B(t)\left(=\frac{B_0}{\sqrt{1-at}}\right)$ applied in the direction of the *Y*-axis. The whole system (fluid and plates) rotates in unison with angular velocity $\left(\Omega^* = \omega j/(1-at)\right)$about the *Y*-axis. The time-dependent gap between the parallel plates is defined by:

$$h(t) = H(1-at)^{1/2} \tag{1}$$

Here the preliminary position of the upper plate is H at $t = 0$ and a is a characteristic frequency parameter with dimension of (time)$^{-1}$ and $at < 1$. The following assumptions are invoked in order to construct the rotating electromagnetohydrodynamic (EMHD) model:

a) A three-dimensional model is considered with the plates in the *X*-*Z* plane.
b) The fluid temperature and concentration are not considered in this model.
c) Electric field is in the *X*-direction and its effect is considered in the *X*-momentum equation.
d) There is no slippage at the interior surfaces of the plate wall.
e) All extra body forces are disregarded.
f) The plate's suction/injection is included.

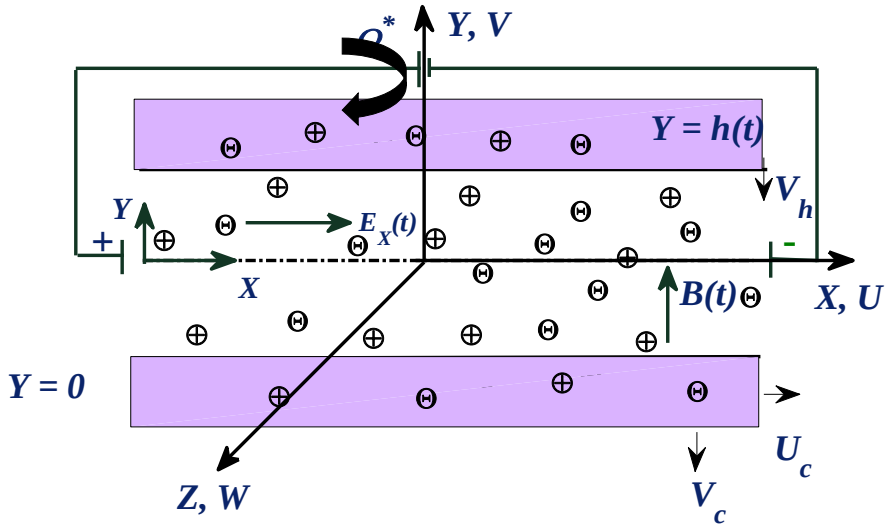

Figure 1: Geometry of the EMHD rotating squeeze flow problem

2.1 The governing equations

The conservation equations describing the flow are the continuity and momentum equations which following [42] are:

$$\frac{\partial U}{\partial X}+\frac{\partial V}{\partial Y}=0, \tag{2}$$

$$\rho\left(\frac{\partial U}{\partial t}+U\frac{\partial U}{\partial X}+V\frac{\partial U}{\partial Y}+\frac{2\omega}{1-at}W\right)=-\frac{\partial P}{\partial X}+\mu\left(\frac{\partial^2 U}{\partial X^2}+\frac{\partial^2 U}{\partial Y^2}\right)-\sigma B^2(t)U+\rho_e E_X(t), \tag{3}$$

$$\rho\left(\frac{\partial V}{\partial t}+U\frac{\partial V}{\partial X}+V\frac{\partial V}{\partial Y}\right)=-\frac{\partial P}{\partial Y}+\mu\left(\frac{\partial^2 V}{\partial X^2}+\frac{\partial^2 V}{\partial Y^2}\right), \tag{4}$$

$$\rho\left(\frac{\partial W}{\partial t}+U\frac{\partial W}{\partial X}+V\frac{\partial W}{\partial Y}-\frac{2\omega}{1-at}U\right)=\mu\left(\frac{\partial^2 W}{\partial X^2}+\frac{\partial^2 W}{\partial Y^2}\right)-\sigma B^2(t)W. \tag{5}$$

Here (U,V,W)denote the velocity components along the (X,Y) directions respectively, $\rho$is density, P is pressure, $\mu$is dynamic viscosity, B_0 is magnetic field and σ is electrical conductivity. The applied electric field $E_X(t)$can be defined as:

$$E_X(t)=\frac{E_x}{1-at}, \tag{6}$$

2.2. Electrical potential

The electrical potential as a result of the electrical double layer (EDL) is given by the Poisson equation at the internal surfaces of the parallel plates [27-29]:

$$\boldsymbol{\nabla^2 E}=-\frac{\boldsymbol{\rho_e}}{\boldsymbol{\varepsilon_{ef}}}, \tag{7}$$

Here ε_{ef} is the permittivity or the dielectric constant of the ionic electrolytic solution. In a symmetric electrolyte solution, the number of ions of type-*i*, denoted by the symbol n_i , follow the equilibrium Boltzmann distribution equation:

$$n_i=n_{i0}\,exp\left(-\frac{z_i eE}{k_B T_H}\right), \tag{8}$$

Here T_H, e , k_B, n_{i0} and z_i are the absolute temperature, electron charge, Boltzmann constant, bulk ionic concentration and the valence of type-*i* ions, respectively.

For a symmetric electrolyte of value $\tilde{z}$, the net volume charge density (ρ_e) is connected to the *overall concentration* and the difference between anions and cations.

$$\rho_e=ze(n_+-n_-). \tag{9}$$

Inserting Eqn. (8) into Eqn. (9), we obtain:

$$\rho_e = -2zen_0\, sinh\left(\frac{zeE}{k_B T_H}\right). \tag{10}$$

Substituting the value of charge density (ρ_e) from (Eqn. (7)) into the Poisson equation (Eqn. (10)) produces the following differential equation:

$$\frac{d^2E}{dY^2} = \frac{2zen_0}{\varepsilon_{ef}} sinh\left(\frac{zeE}{k_B T_H}\right), \tag{11}$$

2.3 Dimensional Boundary conditions

The prescribed boundary conditions for the proposed problem at the upper and lower plates are respectively defined by:

$$\begin{gathered} U = 0, V = V_h = \frac{dh}{dt}, W = 0, E = \tilde{\xi} atY = h(t), \\ U = U_c = \frac{aX}{2(1-at)}, V = V_c = -\frac{V_0}{\sqrt{1-at}}, W = 0, E = 0 atY = 0. \end{gathered} \tag{12}$$

3. SCALING ANALYSIS

To render the governing Eqns. (1)-(5) and (13)-(14) into non-dimensional form, the following similarity transformations are now defined:

$$\left.\begin{aligned} &U = U_c f'(\eta), V = \frac{-aH}{2\sqrt{1-at}} f(\eta), W = U_c g(\eta) \\ &P = \frac{\mu}{X} U_c p(\eta), E = \frac{ze\Phi}{k_B T_H}, \eta = \frac{Y}{H\sqrt{1-at}}. \end{aligned}\right\} \tag{13}$$

The non-dimensional forms of the momentum Eqns. (3)-(5) emerge as:

$$S(2f' + \eta f'' + (f')^2 - ff'' + \Omega g) + M^2 f' - f''' = \frac{\mu aX}{2H^2(1-at)^2}\left(-\frac{\partial P}{\partial X} + \frac{\rho_e E_x}{(1-at)}\right), \tag{14}$$

$$S(f + \eta f' - ff') - f'' = \frac{2H(1-at)^{3/2}}{\mu a}\frac{\partial P}{\partial Y}, \tag{15}$$

$$g'' - S(2g + \eta g' - fg' + gf' - \Omega f') - M^2 g = 0, , \tag{16}$$

By eliminating the pressure term and differentiating Eqn. (15) w.r.t ' X ' and Eqn. (14) w.r.t Y then Eqn. (15) becomes:

$$\frac{\partial^2 P}{\partial X \partial Y} = 0 \tag{17}$$

In due course, Eqn. (14) may then be written as:

$$f''''-S\left(3f''+\eta f'''-ff'''+f''f'+\Omega g'\right)-M^2 f''+Ue\,m^2\cosh\left(\Phi\right)=0, \tag{18}$$

The *electrical potential equation* can be derived via Eqn. (12) as follows:

$$\Phi'' - m^2\, sinh(\Phi) = 0. \tag{19}$$

By virtue of Eqn. (15), the *pressure gradient* can also be determined as:

$$\frac{dp}{d\eta} = S(f + \eta f' - ff') - f'', \tag{20}$$

The associated dimensionless boundary conditions assume the form:

$$\begin{aligned} f(0) = \beta, f'(0) = 1, g(0) = 0, \Phi(0) = 0 \\ f(1) = 1, f'(1) = 0, g(1) = 0, \Phi(1) = \xi \end{aligned} \tag{21}$$

Here $S = \frac{a\rho H^2}{2\mu}$is the squeezing number, $M = HB_0\sqrt{\frac{\sigma}{\mu}}$is the Hartmann number (ratio of magnetic Lorentz force to viscous hydrodynamic force), $\xi = \frac{ze\tilde{\xi}}{k_B T_H}$is the zeta potential parameter, $\Omega = \frac{2\omega}{a}$is the rotation parameter, $\beta = \frac{2V_0}{aH}$ is the plate suction parameter, $Ue = \frac{1}{aX}U_{hs}$ is electric field parameter where $U_{hs} = -\frac{2k_B T_H \varepsilon_{ef} E_x}{\mu ze}$ denotes the Helmholtz-Smoluchowski velocity and $m^2 = K^2H^2(1-at)$ is electroosmosis parameter where $K^2 = -\frac{2z^2e^2n_0}{\varepsilon_{ef}k_B T_H}$ is the Debye-Hückel parameter.

The dimensional form of upper plate (wall) coefficient of skin friction may be defined as follows:

$$C_f = \frac{\mu}{\rho v^2}\left(\frac{\partial U}{\partial Y}\right)_{Y=h(t)}, \tag{22}$$

Using Eqn. (12) in Eqn. (19), we obtain the *dimensionless form* of skin friction coefficient (dimensionless wall shear stress) as follows:

$$\frac{H^2}{X^2}(1-at)R_{ex}C_f = f''(1). \tag{23}$$

where, $v_H = -\frac{aH}{2\sqrt{1-at}}$, and $R_{ex} = \frac{2\rho {v_H}^2 X\sqrt{1-at}}{aH\mu}$ is the local Reynolds numbers.

4. SEMI ANALYTICAL SOLUTION OF THE PROBLEM

4.1 Electrical potential equation

According to standard practice, the Poisson-Boltzmann distribution may be linearized by decreasing the tiny zeta potentials that are generated by most ionic solutions to less than or equal to 25mV. As a result, and Eqn. (19), we get:

$$\Phi'' - m^2\Phi = 0. \tag{24}$$

Then the analytical solution of *electrical potential equation* can be derived via Eqn. (24) with corresponding boundary condition (21) as follows:

$$\Phi = \frac{\xi \sinh(m\eta)}{\sinh(m)}, \tag{25}$$

4.2 Solution of momentum equations

The Homotopy perturbation technique [59-61] can be used to solve the coupled differential equations (16-18), we built the following equation as

$$H(f,\tilde{p}) = (1-\tilde{p})\big(L(f) - L(f_0)\big) + \tilde{p}\,(L(f) - S\eta f''' + Sff''' - Sf''f' - S\Omega g'), \tag{26}$$

$$H(g,\tilde{p}) = (1-\tilde{p})\big(L(g) - L(g_0)\big) + \tilde{p}\,(L(g) - S\eta g' + Sfg' - Sgf' - S\Omega f'), \tag{27}$$

Let us write

$$f = f_0 + \tilde{p}\,f_1 + \tilde{p}f_2 \ldots, \tag{28}$$

$$g = g_0 + \tilde{p}\,g_1 + \tilde{p}g_2 \ldots, \tag{29}$$

It is possible to write the solution of Eqs. (16) and (18) explicitly as for $\tilde{p} \to 1$ up to the first few iterations.

$$f = C_1 + C_2 y + C_3 \mathrm{e}^{-a_2 y} + C_4 \mathrm{e}^{a_2 y} - a_4(\mathrm{e}^{-my} + \mathrm{e}^{my}) + (e^{(-y(a_2+m))})(16C_3 S a_2^8 a_4$$
$$+ 32C_5 a_2^8 m e^{(y(a_2+m))} - 5C_3 S m^7 e^{(my)} + 32C_7 a_2^8 m e^{(my)} - 5C_4 S m^7 e^{(y(2a_2+m))}$$
$$+ 32C_8 a_2^8 m e^{(y(2a_2+m))} - 8C_5 a_2^2 m^7 e^{(y(a_2+m))} + 48C_5 a_2^4 m^5 e^{(y(a_2+m))}$$
$$- 72C_5 a_2^6 m^3 e^{(y(a_2+m))} - 8C_8 a_2^2 m^7 e^{(my)} - 72C_7 a_2^6 m^3 e^{(my)} - 8C_8 a_2^2 m^7 e^{(y(2a_2+m))}$$
$$+ 48C_8 a_2^4 m^5 e^{(y(2a_2+m))} - 72C_8 a_2^6 m^3 e^{(y(2a_2+m))} + 64 S a_2^6 a_4 m e^{(y(a_2+2m))}$$
$$- 8C_6 a_2^2 m^7 y e^{(y(a_2+m))} + 48C_6 a_2^4 m^7 y e^{(y(a_2+m))} - 72C_6 a_2^6 m^3 y e^{(y(a_2+m))}$$
$$+ 30C_3 S a_2^2 m^5 e^{(my)} - 45C_3 S a_2^4 m^3 e^{(my)} + 32 S a_2^2 a_4 m^5 e^{(a_2 y)} - 144 S a_2^4 a_4 m^3 e^{(a_2 y)}$$
$$+ 30C_4 S a_2^2 m^5 e^{(y(2a_2+m))} - 45C_4 S a_2^4 m^3 e^{(y(2a_2+m))} + 32 S a_2^2 a_4 m^5 e^{(y(a_2+2m))}$$
$$- 144 S a_2^4 a_4 m^3 e^{(y(a_2+2m))} - 16C_4 S a_2^8 a_4 e^{(2y(a_2+m))} - 56C_3 S a_2^7 a_4 m$$
$$+ 7C_2 C_3 S m^7 e^{(my)} + 32C_6 a_2^8 m y e^{(y(a_2+m))} + 16C_4 S a_2^8 a_4 e^{((2a_2 y))}$$
$$- 16C_3 S a_2^8 a_4 e^{(2my)} + 20C_3 S a_2^6 m e^{(my)} + 7C_2 C_4 S m^7 e^{(y(2a_2+m))} + 64 S a_2^6 a_4 m e^{(a_2 y)}$$
$$- 8C_3 S a_2^2 a_4 m^6 + 40C_3 S a_2^3 a_4 m^5 - 64C_3 S a_2^4 a_4 m^4 + 16C_3 S a_2^5 a_4 m^3$$
$$+ 56C_3 S a_2^6 a_4 m^2 + 20C_4 S a_2^6 m e^{(y(2a_2+m))} - 2C_3 S a_2^2 m^7 y^2 e^{(my)}$$
$$+ 12C_3 S a_2^4 m^5 y^2 e^{(my)} + 18C_3 S a_2^6 m^3 y^2 e^{(my)} + 2C_1 C_3 S a_2 m^7 e^{(my)}$$
$$- 8C_1 C_3 S a_2^7 m e^{(my)} - 28C_2 C_3 S a_2^6 m e^{(my)} - 96C_2 S a_2^6 a_4 m e^{(a_2 y)}$$
$$+ 56C_4 S a_2^7 a_4 m e^{(a_2 y)} - 2C_4 S a_2^2 m^7 y^2 e^{(y(2a_2+m))} + 12C_4 S a_2^4 m^5 y^2 e^{(y(2a_2+m))}$$
$$- 18C_4 S a_2^6 m^3 y^2 e^{(y(2a_2+m))} - 56C_3 S a_2^7 a_4 m e^{(2my)} - 2C_1 C_4 S a_2 m^7 e^{(y(2a_2+m))}$$
$$+ 8C_1 C_4 S a_2^7 m e^{(y(2a_2+m))} - 28C_2 C_4 S a_2^6 m e^{(y(2a_2+m))} - 10C_3 S a_2 m^7 y e^{(my)}$$
$$+ 40C_3 S a_2^7 m y e^{(my)} - 96C_2 S a_2^6 a_4 m e^{(y(a_2+2m))} + 8C_4 S a_2^2 a_4 m^6 e^{(2y(a_2+m))} -$$

$$40C_4 S a_2^3 a_4 m^5 e^{(2y(a_2+m))} + 64C_4 S a_2^4 a_4 m^4 e^{(2y(a_2+m))} - 16C_4 S a_2^5 a_4 m^3 e^{(2y(a_2+m))}$$
$$- 56C_4 S a_2^6 a_4 m^2 e^{(2y(a_2+m))} + 10C_4 S a_2 m^7 y e^{(2y(a_2+m))} - 40C_4 S a_2^7 m y e^{(2y(a_2+m))}$$
$$- 12C_1 C_3 S a_2^3 m^5 e^{(my)} + 18C_1 C_3 S a_2^5 m^3 e^{(my)} - 42C_2 C_3 S\, a_2^2 m^5 e^{(my)}$$
$$+ 63C_2 C_3 S a_2^4 m^3 e^{(my)} - 8C_1 S\, a_2^2 a_4 m^6 e^{(a_2 y)} + 40C_1 S\, a_2^4 a_4 m^4 e^{(a_2 y)}$$
$$- 32C_1 S\, a_2^6 a_4 m^2 e^{(a_2 y)} - 40C_2 S\, a_2^2 a_4 m^5 e^{(a_2 y)} + 184C_2 S\, a_2^4 a_4 m^3 e^{(a_2 y)}$$
$$- 8\, C_4 S\, a_2^2 a_4 m^6 e^{(2a_2 y)} - 40\, C_4 S\, a_2^3 a_4 m^5 e^{(2a_2 y)} - 64\, C_4 S\, a_2^4 a_4 m^4 e^{(2a_2 y)}$$
$$- 16\, C_4 S\, a_2^5 a_4 m^3 e^{(2a_2 y)} + 56\, C_4 S\, a_2^6 a_4 m^2 e^{(2a_2 y)} + 8\, C_3 S\, a_2^2 a_4 m^6 e^{(2my)}$$
$$+ 40\, C_3 S\, a_2^3 a_4 m^5 e^{(2my)} + 64\, C_3 S\, a_2^4 a_4 m^4 e^{(2my)} + 16C_3 S\, a_2^5 a_4 m^3 e^{(2my)}$$
$$- 56\, C_3 S\, a_2^6 a_4 m^2 e^{(2my)} + 12C_1 C_4 S a_2^3\, m^5 e^{(y(2a_2+m))} - 18C_1 C_4 S a_2^3\, m^5 e^{(y(2a_2+m))}$$
$$- 42C_2 C_4 S a_2^2\, m^5 e^{(y(2a_2+m))} + 63C_2 C_4 S a_2^4\, m^3 e^{(y(2a_2+m))} + 60C_3 S\, a_2^3 m^5 y e^{(my)}$$
$$- 90\, C_3 S\, a_2^5 m^3 y e^{(my)} + 8C_3 S\, a_2^8 m y^2 e^{(my)} + 8C_1 S\, a_2^2 a_4 m^6 e^{(a_2+2m)}$$
$$- 40\, C_1 S\, a_2^4 a_4 m^4\, e^{(y(a_2+2m))} + 32\, C_1 S\, a_2^6 a_4 m^4\, e^{(y(a_2+2m))}$$
$$- 40C_2 S\, a_2^2 a_4 m^5\, e^{(y(a_2+2m))} + 184C_2 S\, a_2^4 a_4 m^3\, e^{(y(a_2+2m))} + 8\, S a_2^2 a_4 m^6\, e^{(a_2 y)}$$
$$- 40 S a_2^4 a_4 m^4 y\, e^{(a_2 y)} + 32 S a_2^6 a_4 m^2 y\, e^{(a_2 y)} - 60C_4 S a_2^3 m^5 y\, e^{(y(2a_2+m))}$$
$$+ 90C_4 S a_2^5 m^3 y\, e^{(y(2a_2+m))} + 8C_4 S a_2^8 m y^2\, e^{(y(2a_2+m))} - 8 S a_2^2 a_4 m^6 y e^{(y(a_2+2m))}$$
$$+ 40 S a_2^4 a_4 m^4 y e^{(y(a_2+2m))} - 32 S a_2^6 a_4 m^2 y e^{(y(a_2+2m))} + 56C_4 S a_2^7 a_4 m e^{(2y(a_2+m))}$$
$$+ 4C_1 C_4 S a_2^2\, m^7 y e^{(y(2a_2+m))} - 24C_1 C_4 S a_2^4\, m^5 y e^{(y(2a_2+m))}$$
$$+ 36C_1 C_4 S a_2^6\, m^3 y e^{(y(2a_2+m))} +$$

$$84C_2 C_4 S a_2^3 m^5 y e^{(y(2a_2+m))} - 126C_2 C_4 S a_2^5 m^3 y e^{(y(2a_2+m))} - 8C_2 C_4 S a_2^8 m y^2 e^{(y(2a_2+m))} +$$
$$8C_2 S a_2^2 a_4 m^6 y e^{(y(a_2+2m))} - 40C_2 S a_2^4 a_4 m^4 y e^{(y(a_2+2m))} + 32C_2 S a_2^6 a_4 m^2 y e^{(y(a_2+2m))} +$$
$$2C_2 C_3 S a_2^2 m^7 y^2 e^{(my)} - 12C_2 C_3 S a_2^4 m^5 y^2 e^{(my)} + 18C_2 C_3 S a_2^6 m^3 y^2 e^{(my)} +$$
$$2C_2 C_4 S a_2^2 m^7 y^2 e^{(y(2a_2+m))} - 12C_2 C_4 S a_2^4 m^5 y^2 e^{(y(2a_2+m))} + 18C_2 C_4 S a_2^6 m^3 y^2 e^{(y(2a_2+m))} -$$

$16C_1C_3Sa_2^8mye^{(my)} + 14C_2C_3Sa_2m^7ye^{(my)} - 56C_2C_3Sa_2^7mye^{(my)} - 16C_1C_4Sa_2^8mye^{(y(2a_2+2m))} - 14C_2C_4Sa_2m^7e^{(y(2a_2+2m))} + 56C_2C_4Sa_2^7mye^{(y(2a_2+2m))} + 4C_1C_3Sa_2^2m^7ye^{(my)} - 24C_1C_3Sa_2^4m^7ye^{(my)} + 36C_1C_3Sa_2^6m^3ye^{(my)} - 84C_2C_3Sa_2^3m^5ye^{(my)} + 126C_2C_3Sa_2^5m^3ye^{(my)} - 8C_2C_3Sa_2^8my^2e^{(my)} - 8C_2Sa_2^2a_4m^6ye^{(a_2y)} + 40C_2Sa_2^4a_4m^4ye^{(a_2y)} - 32C_2Sa_2^6a_4m^2ye^{(a_2y)}))/ (8a_2^2m(a_2^2 - m^2)^2(4a_2^2 - m^2)),$ (30)

$$g(y) = C_9e^{-a_{20}y} + C_{10}e^{a_{20}y} - \frac{a_{21}}{a_{20}^2} - \frac{a_{23}e^{-a_2y}}{2(a_{20}^2+a_2a_{20})} + \frac{a_{23}e^{-a_2y}}{2(-a_{20}^2+a_2a_{20})} - \frac{a_{24}e^{a_2y}}{2(a_{20}^2+a_2a_{20})} + \frac{a_{24}e^{a_2y}}{2(-a_{20}^2+a_2a_{20})} - \frac{a_{22}y}{a_{20}^2} + \frac{a_{20}a_{25}e^{my}}{-a_{20}^2+a_{20}m^2} + \frac{a_{20}a_{25}e^{-my}}{-a_{20}^2+a_{20}m^2}, \quad (31)$$

The above-mentioned constants are defined in Appendix.

5. NUMERICAL SOLUTION WITH MATLAB AND VALIDATION

The nonlinear coupled dimensionless ordinary differential equations (16, 18, 19) with boundary conditions (Eqn. 21) do not permit analytical solutions. Therefore, a numerical solution is obtained using the shooting technique in MATLAB [53]. This quadrature procedure reduces the differential equations of higher order i.e. the momentum and electrical potential Eqns. (16, 18, 19) to *first-order* equations:

$$\left.\begin{aligned} y_1 &= f; \\ y_2 &= f' \\ y_3 &= f'' \\ y_4 &= f''' \\ y_4' &= S(3y_3 + \eta y_4 - y_1y_4 + y_3y_2 + \Omega y_6) + M^2y_3 - Uem^2\,cosh(y_7) \\ y_5 &= g \\ y_6 &= g' \\ y_6' &= S(2y_5 + \eta y_6 - y_1y_6 + y_5y_2 - \Omega y_2) + M^2y_5 \\ y_7 &= \Phi \\ y_8 &= \Phi' \\ y_8' &= m^2\,sinh(\Phi) \end{aligned}\right\} \quad (32)$$

According to the boundary conditions (21), the corresponding initial conditions are introduced as:

$$\left.\begin{aligned} y_1(0) = \beta, y_2(0) = 1, y_5(0) = 0, y_7(0) = 0 \\ y_3(0) = a_1, y_4(0) = a_2, y_6(0) = a_3, y_7(0) = a_4. \end{aligned}\right\} \quad (33)$$

To implement Eqn. (33), we assume that a_1, a_2, a_3 and a_4 are at $\eta = 0$ at the beginning of the problem. MATLAB software is used to construct a programme based on this approach. Also, the

present boundary conditions $f'(0)=1$ and $f'(1)=0$ are converted into the form of $f''(0)=A$ which is solved by using shooting method. A comparison is conducted between the solutions of Wang **[54]** for Newtonian squeezing flow (a very special case of the present model) and the current MATLAB solution, for values of $f''(1)$ i.e. skin friction (dimensionless wall shear stress or velocity gradient) at the upper plate, for various values of the squeezing parameter, *S* with $M=0; Ue=0;\ A=0;\ \Omega=0$ *and* $\beta=0.$ This data corresponds to absence of magnetic field, electro-osmosis, non-rotation and a non-permeable (solid) plate as considered in the study by Wang [54]. The findings of the proposed model are in good agreement and correlation with the results of Wang [54], which are reported in table -1 of this paper. Excellent correlation was obtained for both small and high values of *S*, confirming confidence in the present MATLAB code. Also, the present MATLAB results have been compared with well-known semi analytical method known as the He Homotopy perturbation technique and are clearly portrayed in **Fig. 2** for fixed value of $\xi=0.5, S=0.5, \beta=0.1, \Omega=0.1, m=1.5, Ue=1$ *and* $M=0.309$. Very good correlation of $f(\eta)$ & $g(\eta)$ are attained between the HPM and MATLAB BVP4c results. Confidence in the present MATLAB solutions is therefore justifiably high.

Table 1 Comparison result of present solution and existing solution [54] for various values of the squeezing parameter, *S* with $M=0; Ue=0;\ A=0;\ \Omega=0$ *and* $\beta=0.$

	Upper plate skin friction $f''(1)$	
S	Wang [54] solution	Present solution
0	-3	-3
0.09403	-3.0665	-3.066372403275870
0.4341	-3.2969	-3.294282184859250
1.1224	-3.714	-3.707994385020350

6. NUMERICAL RESULTS AND DISCUSSION

A detailed parametric study has been conducted to investigate the influence of key emerging parameters i.e. squeezing parameter *S*, Hartmann number *M*, electric field parameter Ue, electroosmosis parameter m, zeta potential parameter ξ, rotation parameter Ω and suction

parameter β on the velocity profiles, pressure gradient, and upper wall skin friction. These are visualized as graphs in **Figs.3-18**. All data has been prescribed carefully based on realistic EMHD lubricating flows [42, 55, 56].

Figs. 3-9 illustrate the evolution of axial velocity and transverse velocity profiles across the entire gap between the parallel plates, for various parameters. **Fig. 3** shows the effect of *S* on the axial velocity $f'(\eta)$ and transverse velocity $g(\eta)$ distributions. Both separating ($S > 0$) and closing ($S < 0$) are examined, which are two important scenarios in lubrication designs. Increase in the value of the squeezing parameter acts to suppress the axial velocity, $f'(\eta)$ in the lower half space of the gap ($0 < \eta < 0.5$) whereas it enhances axial velocity in the upper half space ($0.5 < \eta < 1.0$). A cross-over is computed at the centreline of the gap ($\eta = 0.5$).

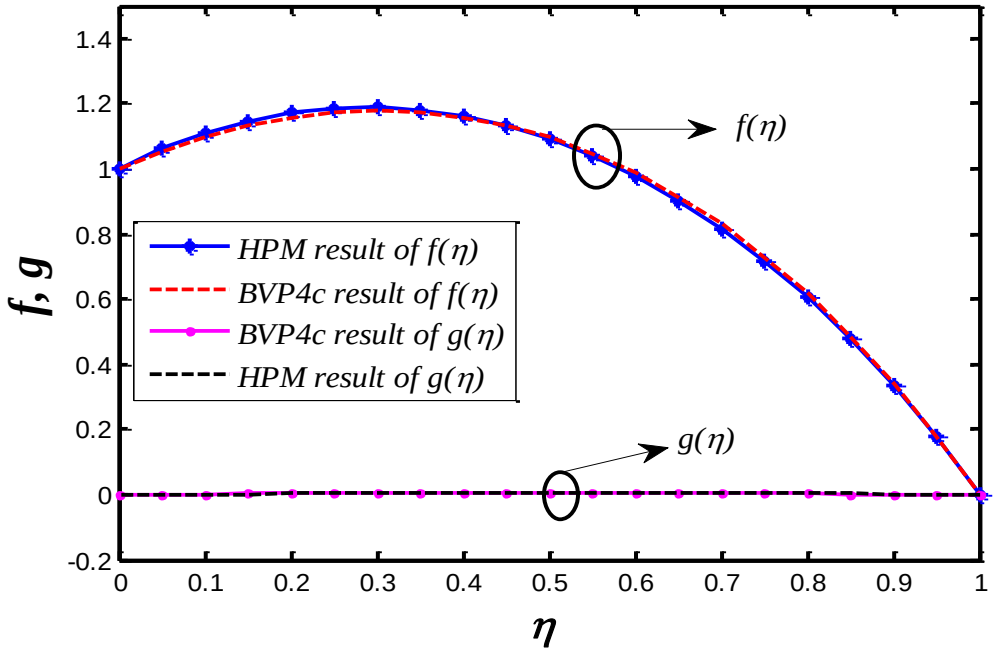

Fig.2 Comparison results between Homotopy Perturbation Method (HPM) and MATLAB BVP4c command for fixed value of $\xi = 0.5, S = 0.5, \beta = 0.1, \Omega = 0.1, m = 1.5, Ue = 1$ and $M = 0.309$.

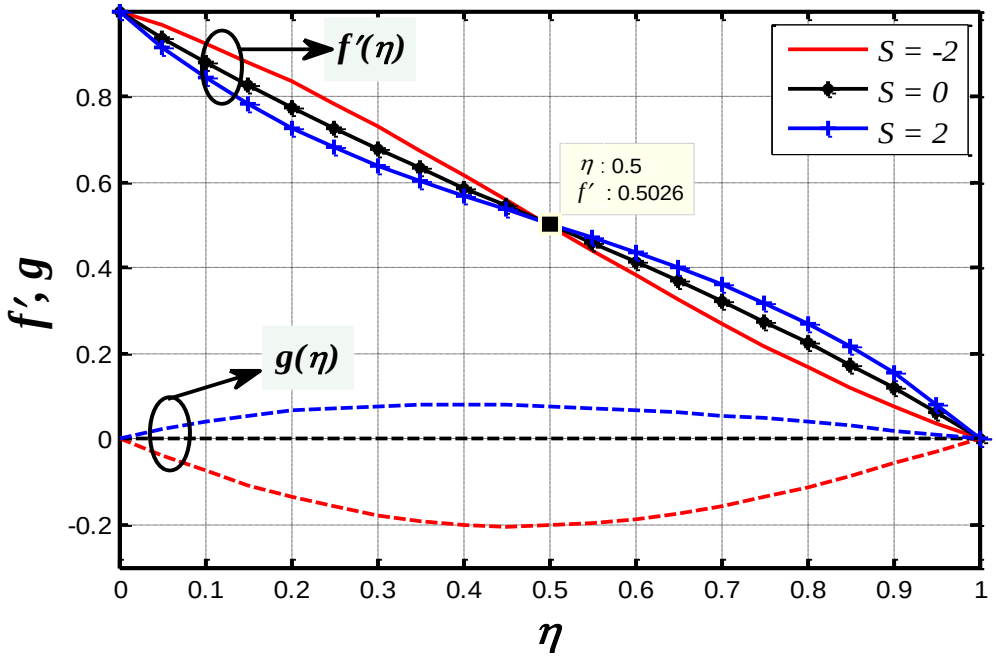

Fig.3 Impact of squeezing parameter S on the axial velocity f' and transverse velocity g for fixed values of $M=1; Ue=1;\ m=1.5; \xi=0.5; \beta=0.5$ and $\Omega=1$.

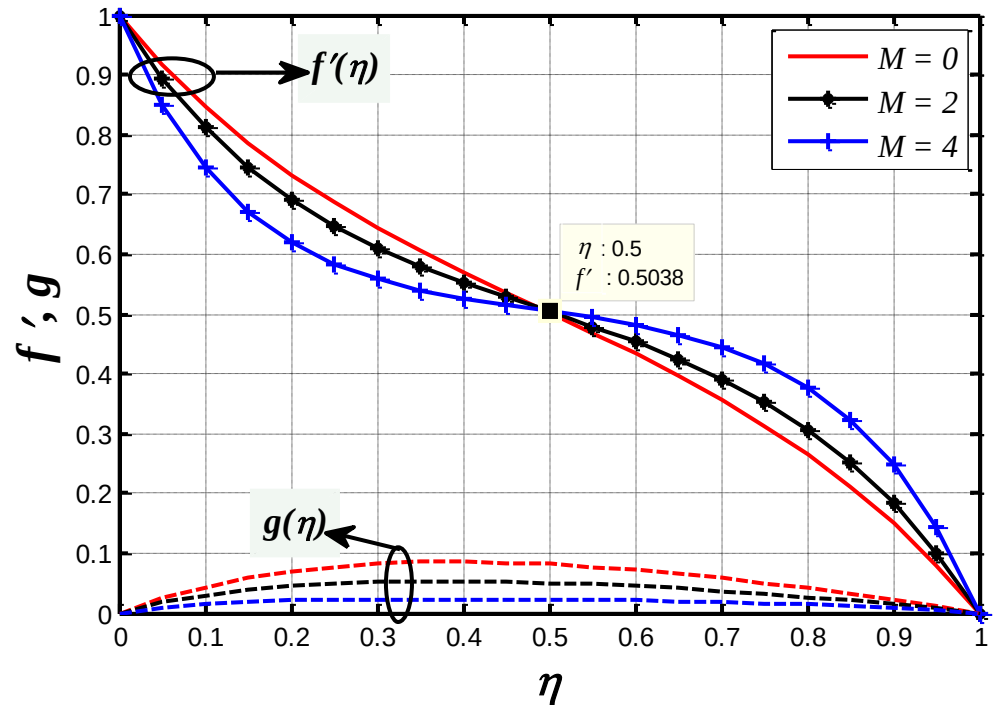

Fig.4 Impact of magnetic parameter M on the axial velocity f' and transverse velocity g for fixed values of $S=2; Ue=1;\ m=1.5; \xi=0.5; \beta=0.5$ and $\Omega=1$.

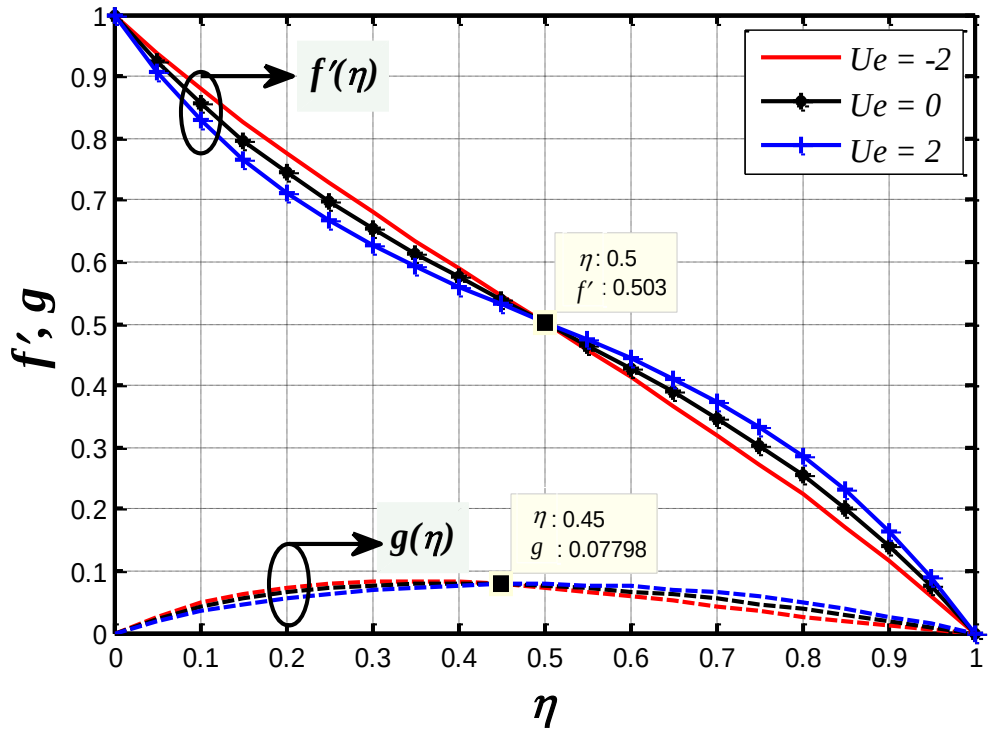

Fig.5 Impact of electric field parameter Ue on the axial velocity f' and transverse velocity g for fixed values of $S=2; M=1; m=1.5; \xi=0.5; \beta=0.5$ and $\Omega=1$.

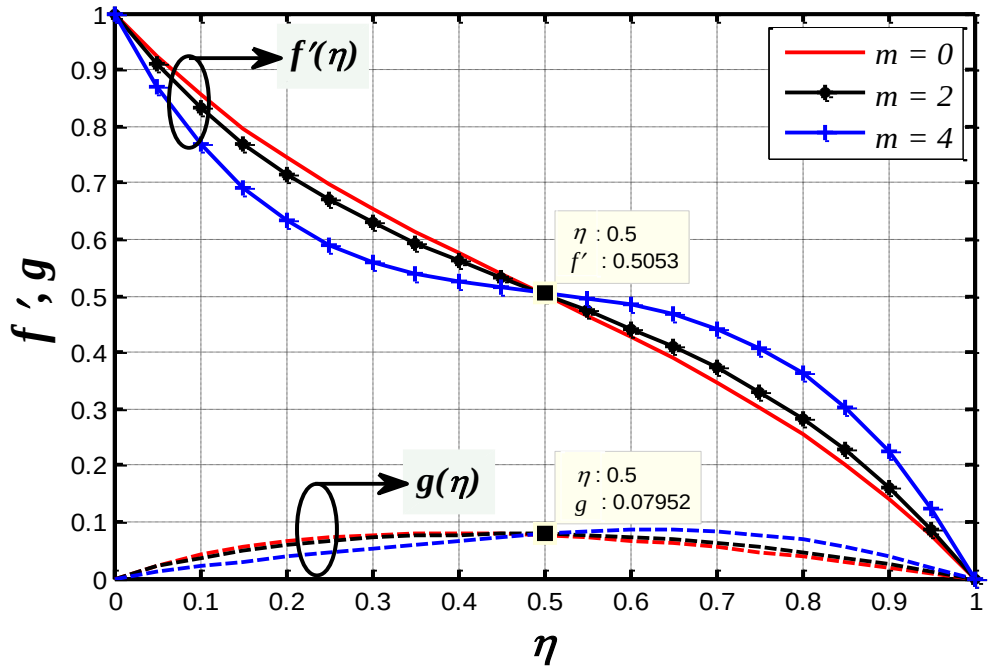

Fig.6 Impact of electroosmosis parameter m on the axial velocity f' and transverse velocity g for fixed values of $S=2; Ue=1; M=1.5; \xi=0.5; \beta=0.5$ and $\Omega=1$.

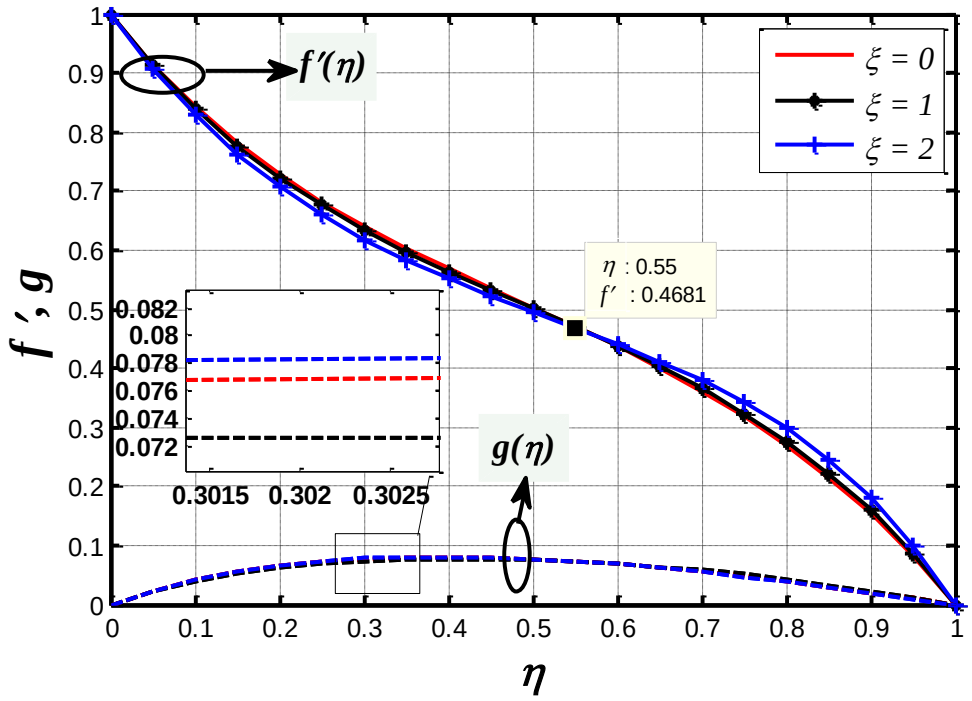

Fig.7 Impact of zeta potential parameter ξ on the axial velocity f' and transverse velocity g for fixed values of $S=2; Ue=1;\ m=1.5; M=1; \beta=0.5$ and $\Omega=1$.

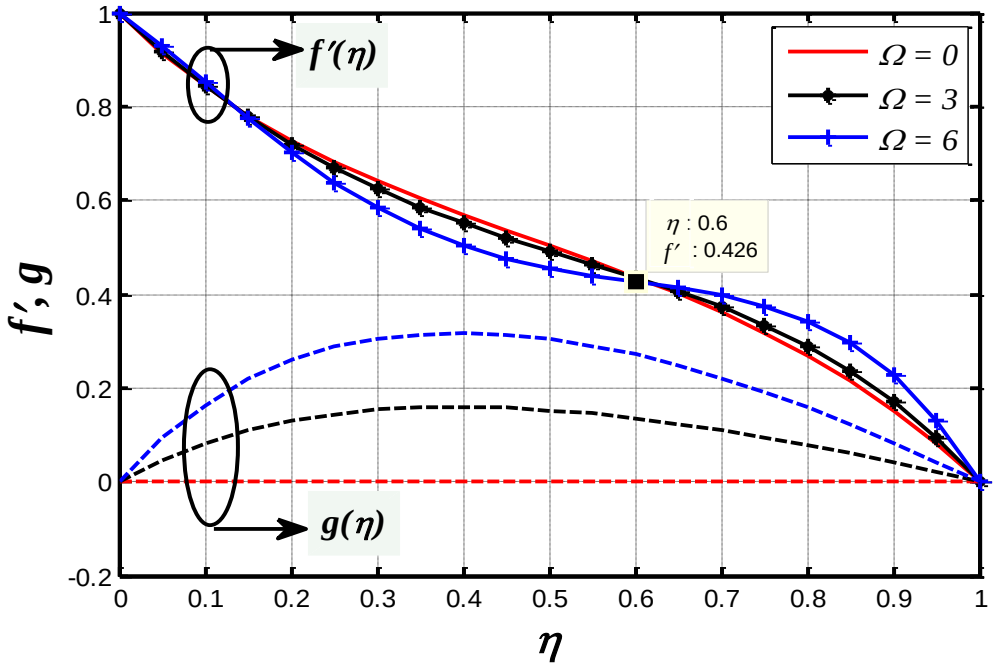

Fig.8 Impact of rotation parameter Ω on the axial velocity f' and transverse velocity g for fixed values of $S=2; Ue=1;\ m=1.5; \xi=0.5; \beta=0.5$ and $M=1$.

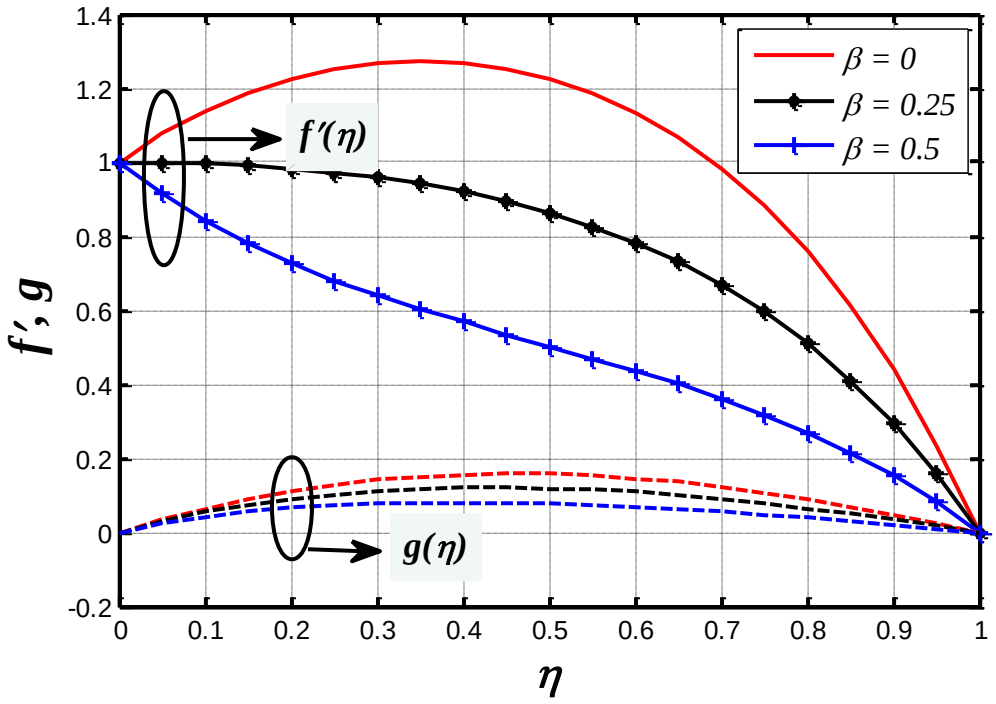

Fig.9 Impact of suction parameter β on the axial velocity f' and transverse velocity g for fixed values of $S=2; Ue=1;\ m=1.5; \xi=0.5; M=1$ and $\Omega=1$.

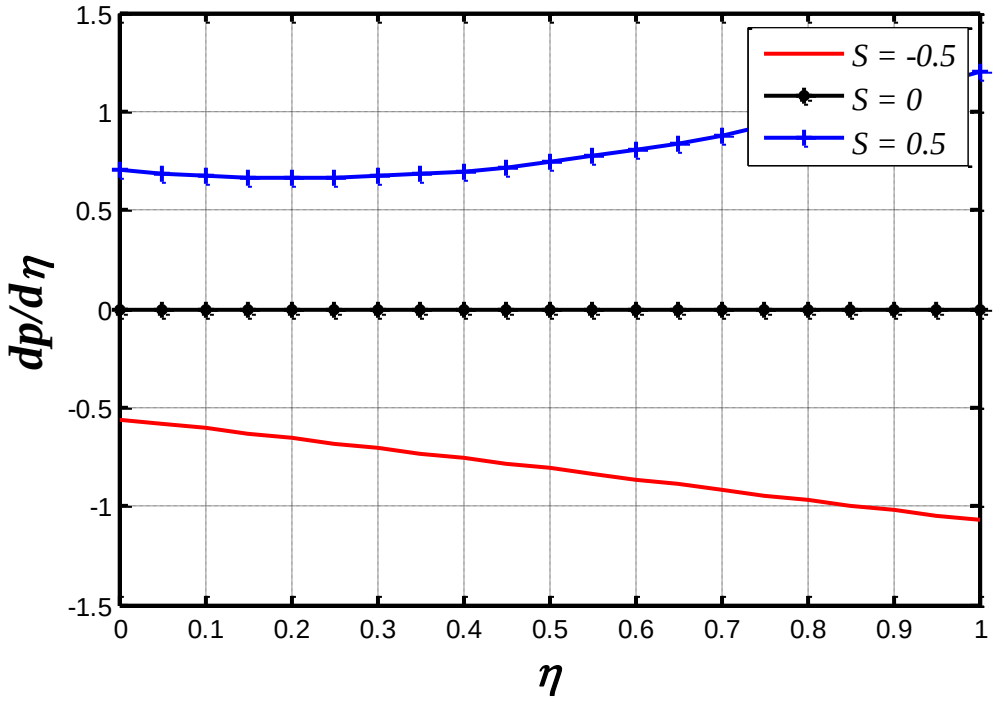

Fig.10 Impact of squeezing parameter S on the pressure gradient $dp/d\eta$ for fixed values of $M=1; Ue=1;\ m=1.5; \xi=0.5; \beta=0.5$ and $\Omega=1$.

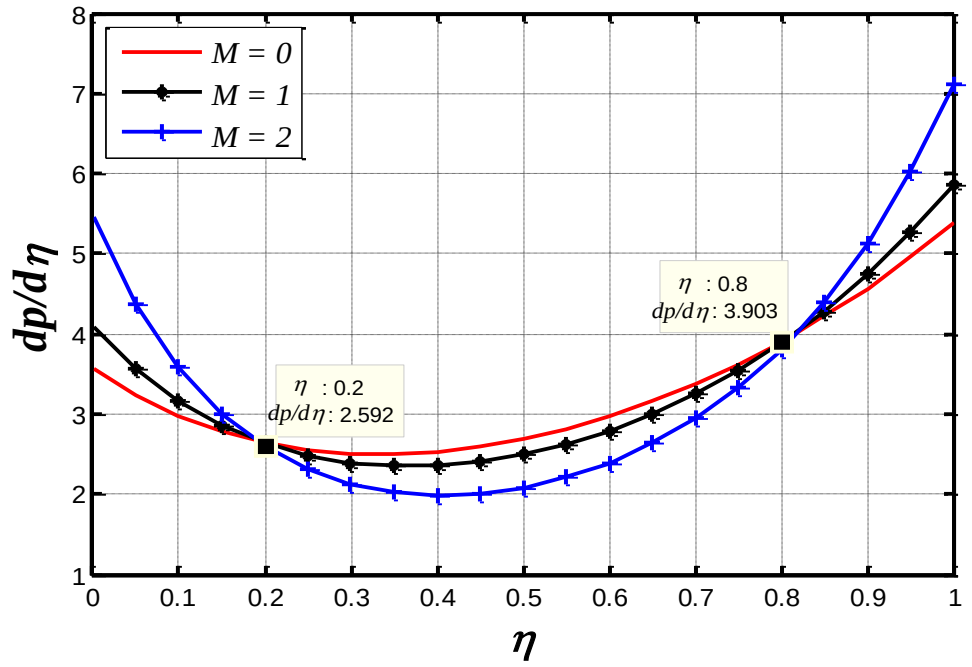

Fig.11 Impact of magnetic parameter M on the pressure gradient $dp/d\eta$ for fixed values of $S=2; Ue=1;\ m=1.5; \xi=0.5; \beta=0.5$ and $\Omega=1$.

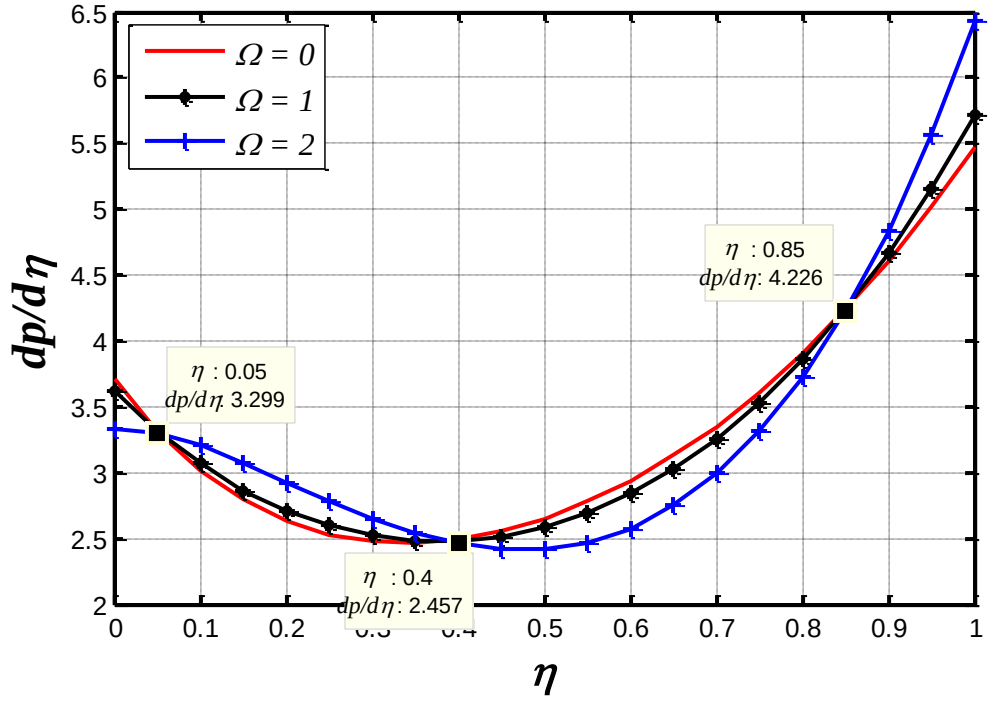

Fig.12 Impact of rotation parameter Ω on the pressure gradient $dp/d\eta$ for fixed values of $M=1; Ue=1;\ m=1.5; \xi=0.5; \beta=0.5$ and $S=2$.

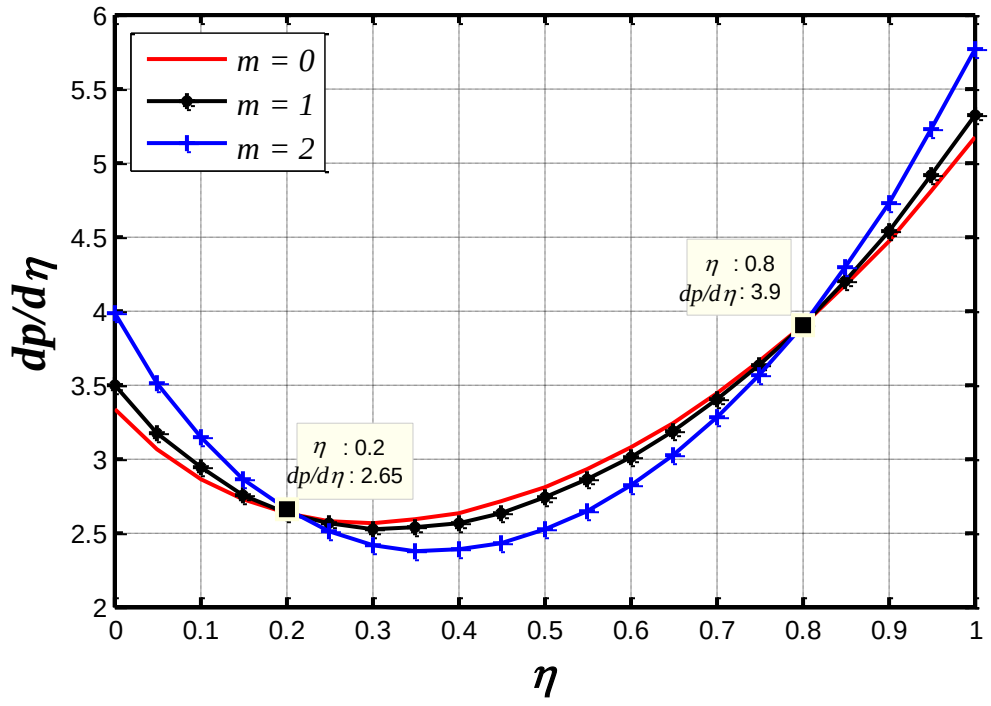

Fig.13 Impact of electroosmosis parameter m on the pressure gradient $dp/d\eta$ for fixed values of $M=1; Ue=1;\ S=2; \xi=0.5; \beta=0.5$ and $\Omega=1$.

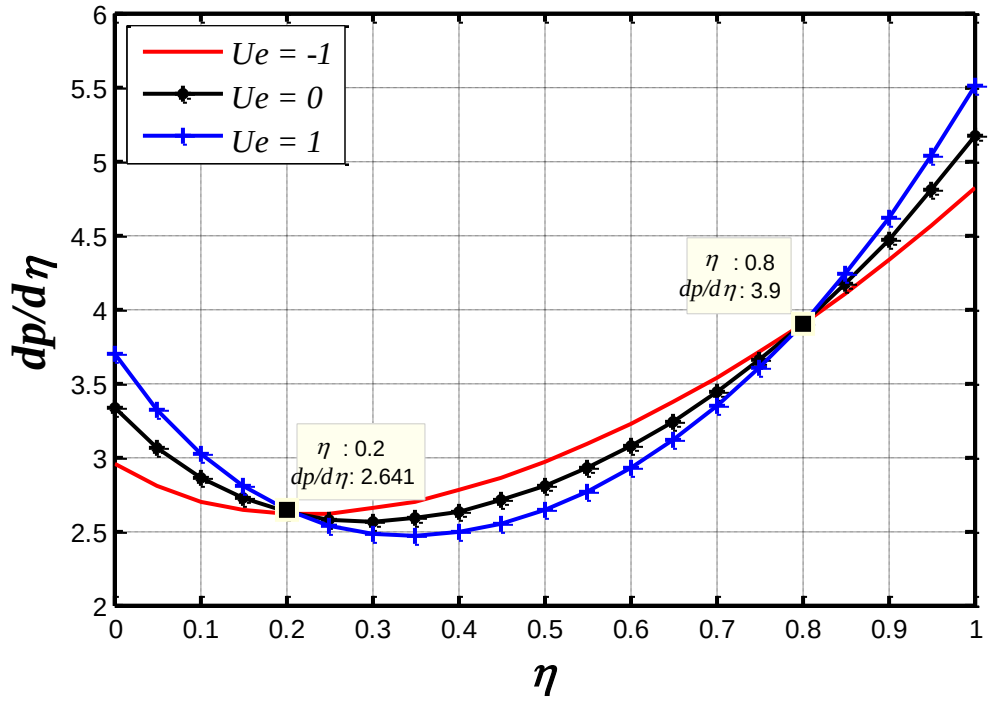

Fig.14 Impact of electric field parameter Ue on the pressure gradient $dp/d\eta$ for fixed values of $M=1; S=2;\ m=1.5; \xi=0.5; \beta=0.5$ and $\Omega=1$.

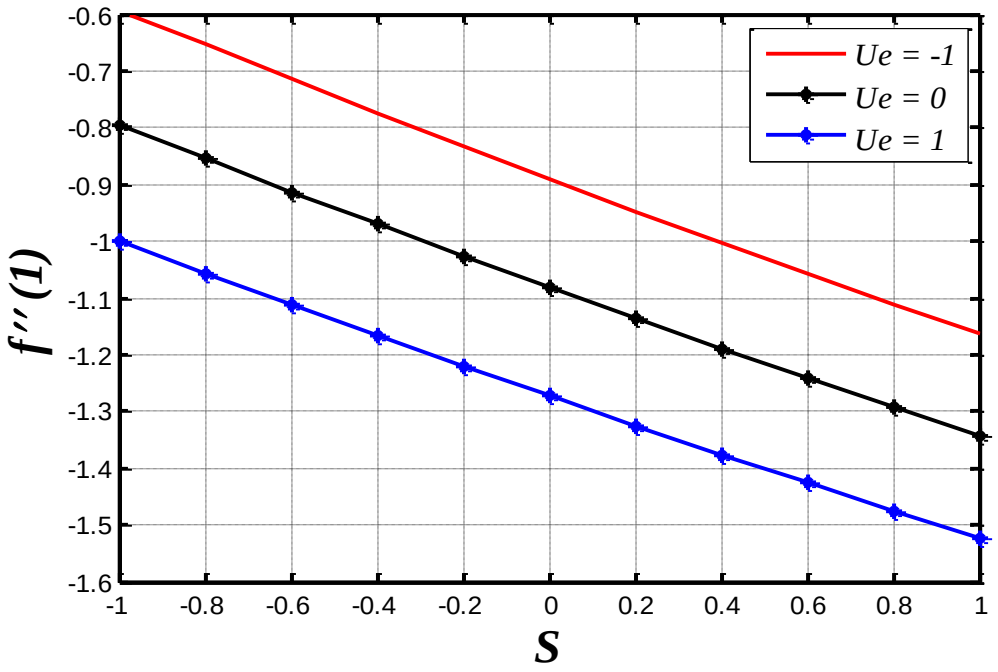

Fig.15 Impact of electric field parameter Ue on the upper wall skin friction $f''(1)$ against S for fixed values of $M=1; m=1.5; \xi=0.5; \beta=0.5$ and $\Omega=1$.

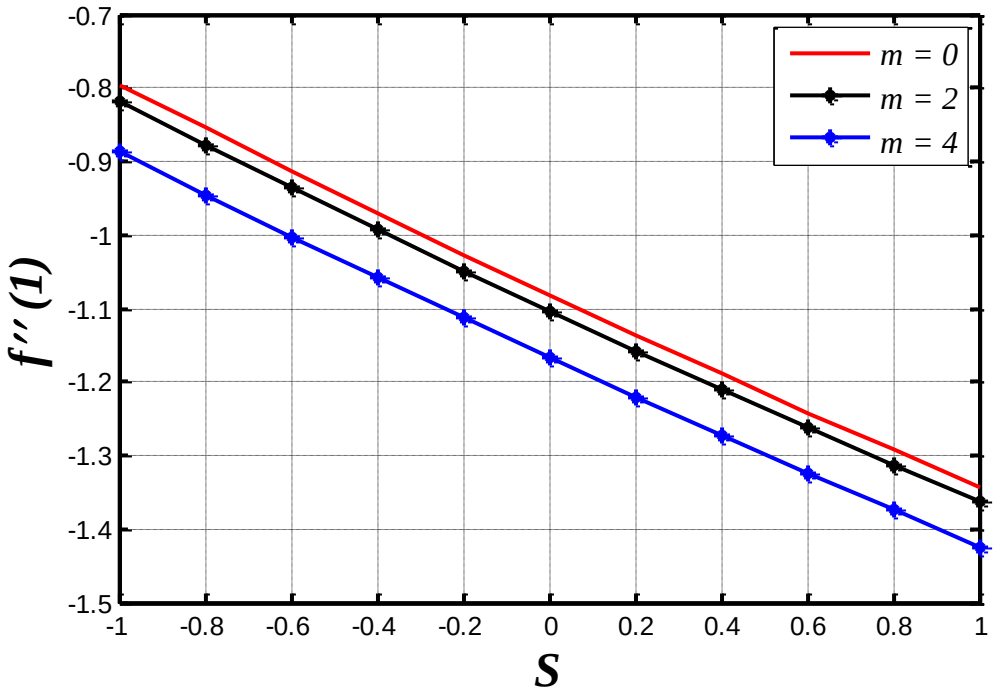

Fig.16 Impact of electroosmosis parameter m, on the upper wall skin friction $f''(1)$ against S for fixed values of $M=1; Ue=1; \xi=0.5; \beta=0.5$ and $\Omega=1$.

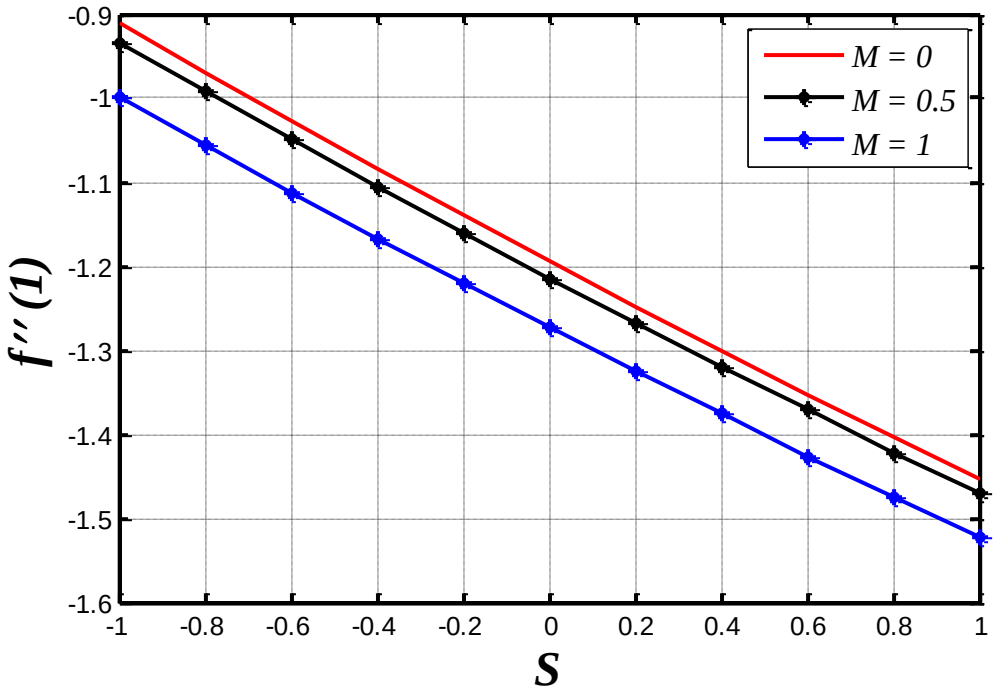

Fig.17 Impact of magnetic parameter M on the upper wall skin friction $f''(1)$ against S for fixed values of $Ue=1;\ m=1.5;\xi=0.5;\beta=0.5$ and $\Omega=1.$

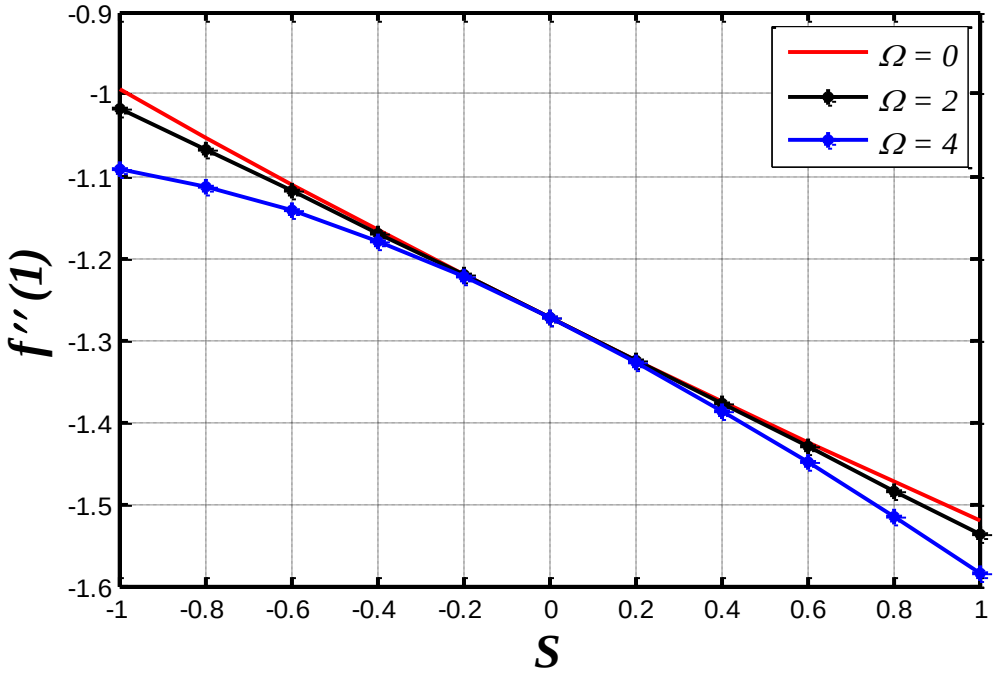

Fig.18 Impact of rotation parameter Ω on the upper wall skin friction $f''(1)$ against S for fixed values of $M=1;Ue=1;\ m=1.5;\xi=0.5$ *and* $\beta=0.5.$

As the plate surfaces move closer together, the fluid is physically constrained under the squeezing force and deceleration is induced in the axial velocity in the lower channel half space. However, momentum is re-distributed by virtue of conservation and this generates acceleration in the upper half space. The squeezing parameter, *S*. features in the modified shear terms in the axial momentum Eqn. (18), viz, $-S(3f'' + \eta f''' - ff''' + f''f' + \Omega g')$. The effect of squeezing ($S < 0$) renders these terms positive which assists the axial flow and results in acceleration in the lower half space. Separating plates ($S > 0$) results in a negative version of the terms and this inhibits the *axial flow* in the lower half space. Also, it is observed from **Fig.3** that positive *S* (separating plates) however, generates a boost in transverse velocity g which is sustained across the entire gap. Transverse flow acceleration is therefore induced with the *plates moving apart*. The opposite effect i. e. flow deceleration accompanies a negative value of *S* (squeezing). Both effects are maximized at the centreline of the gap. Unlike the axial velocity, there is no switch in the topology of the transverse velocity at the mid-point of the gap; the behaviour is consistent at all locations across the gap. There is also significant modification in the terms, $-S(2g + \eta g' - fg' + gf' - \Omega f')$ in the transverse momentum Eqn. (16). In addition, both axial and transverse velocity fields are strongly coupled so there exists a substantial interplay between both velocity components. Acceleration in the axial flow is thereby compensated for by deceleration (retardation) in the transverse flow and vice versa. It is noteworthy that $S = 0$ corresponds to the case where the plates are stationary, and the gap depth is constant; this naturally produces profiles which fall between the $S > 0$ and $S < 0$ cases.

Fig.4 shows the evolution of axial and transverse velocity with Hartmann number, *M*. A strong damping in axial velocity is generated in the lower half space with increment in Hartmann number, indicating that the axial flow is inhibited significantly with stronger magnetic field intensity. This effect is reversed in the upper half space where strong flow acceleration is produced, and a reflective symmetry is computed in the profiles about the mid-point of the channel. This modification in axial velocity response is again attributable to the re-distribution in momentum in the gap. Viscous hydrodynamic force is equivalent to magnetic (Lorentz) body force when $M = 1$, as noted by Cramer and Pai [56]. The impact of magnetohydrodynamics is zero when $M = 0$; this electrically non-conducting case achieves therefore a maximum magnitude in the lower half space whereas it is associated with a minimal magnitude in the upper half space. Therefore, while the Lorentzian magnetohydrodynamic body force, $-M^2 f''$, in Eqn. (18) has an inhibiting effect in the lower half of the gap this body force is assistive in the upper half space. In addition, it is evident in **Fig. 4** that greater Hartmann number i.e. higher intensity of magnetic

field produces a sustained deceleration in the transverse flow across the gap. velocity progressively. The Lorentzian body force in Eqn. (16) i. e. $-M^2 g$, therefore strongly damps the transverse flow at all values of transverse coordinate, η. The non-magnetic case, $M = 0$, produces strong transverse flow acceleration across the gap. It is pertinent also to mention that significantly greater magnitudes are computed for the axial velocity than the transverse velocity, irrespective of location in the gap or the parameter being varied, in Figs. 3 and 4. Furthermore negative velocities are never computed indicating that axial or transverse backflow never arise anywhere in the gap. Axial flow topologies are always decaying from the lower plate to the upper plate, whereas the transverse velocity exhibits a parabolic distribution across the gap with a maximum at the centreline.

Dimensionless axial velocity and transverse velocity patterns for positive and negative values of the electric field parameter *Ue* are shown in **Fig. 5**. The electric field component has a critical role in regulating the squeezing flow. As per the convention adopted in Fig. 1, for which the positive axial direction is from left to right, the electrical field parameter value (electrical field parameter) is *negative*; however, it is *positive* when the electrical field direction is reversed (right to left). Axial velocity is enhanced for negative *Ue* in the lower half space (acceleration) whereas it is depleted in the upper half space (retardation). The contrary behaviour is computed for positive *Ue.* Again, axial velocity decays from the lower plate where it is always a maximum to the upper plate where it is a minimum. Transverse velocity is also found to be elevated in the lower half space, albeit weakly, with negative *Ue* whereas it is suppressed with positive *Ue.* This trend is reversed in the upper half space of the gap. Effectively the orientation of the axial electrical field is responsible for either inducing acceleration or retardation in both velocity components as simulated via the electrical field parameter, $U_{hs} = -\frac{2k_B T_H \varepsilon_{ef} E_x}{\mu z e}$. Significant manipulation in the flow characteristics can be achieved therefore both with magnetic field (as studied earlier in Fig. 4) and the electrical field, which are mutually orthogonal.

Fig. 6 displays the behaviour across the gap of axial and transverse velocity components $\left(f'(\eta)\&g(\eta)\right)$ with variation in electroosmosis parameter, *m*. This critical parameter features in the axial momentum Eqn. (18) in the term, $+Uem^2 cosh(\Phi)$, which couples this equation to the electrical potential Eqn. (19). Furthermore, $m^2 = K^2 H^2 (1 - at)$ where $K^2 = -\frac{2z^2 e^2 n_0}{\varepsilon_{ef} k_B T_H}$ is the Debye-Hückel parameter. There is therefore a powerful influence of electro-osmosis via ionic mobility in the flow on the axial velocity field experienced via *m*, and in turn via coupling of the

axial momentum Eqn. (18) to the transverse momentum Eqn. (16), the transverse velocity field is also indirectly influenced. The electro-osmotic body force effect is negated when $m = 0$. Strong axial flow deceleration is produced in the lower half space of the gap between the plates, $0 \le \eta < 0.5$ with increment in *m*, indicating that ion mobilization encourages axial flow in this zone. However, the contrary response is observed in the upper half space, $0.5 \le \eta \le 1$ where higher values of m manifest in a significant axial flow acceleration. Axial velocity profiles also become increasingly parabolic with greater *m* values. Axial flow velocities will generally decrease near the lower plate as the thickness of the electric double layer (EDL) is reduced i. e. corresponding to an increase in electroosmotic parameter, *m,* since EDL and m are inversely proportional. The opposite effect will be induced near the upper plate. Transverse velocity is also damped in the lower half space with greater electroosmotic parameter, *m, (i. e. thinner EDL) although the effect is less prominent than in the axial velocity.* A weak acceleration in transverse flow is computed in the upper half space of the gap. Overall, the axial flow demonstrates a much greater sensitivity to the electro-osmotic parameter since it is the dominant (bulk) flow in the regime and is primarily influenced by ionic distributions which in turn are affected by the applied voltage across the gap and the axial field orientation.

The impact of the zeta potential parameter ξ on the velocity profiles $\left(f'(\eta) \& g(\eta)\right)$ is illustrated in **Fig. 7**. The zeta potential parameter $\xi = \frac{\tilde{z}e\tilde{\xi}}{k_B \tilde{T}_{\tilde{H}}}$ arises in the top plate boundary condition viz, $\Phi(1) = \xi$. It is known that in bio-microfluidics, large zeta potential can influence the flow [28, 57] in electro-osmotic systems, although lower and intermediate values generate mild modifications in velocity fields. The values examined here i.e. ξ = 0 (vanishing zeta potential), 1, 2 are not excessively high. However, under the action of the axial electrical field, E_x, with fixed charges on the inner surfaces of the plates, positively charged cations from the bulk solution are attracted creating a double layer with positive charge density that decreases exponentially as the distance from the plate increases. A potential difference is mobilized in close proximity to the plate surface and is known as the zeta potential which is intimately linked to the electrostatic nature of the plate surfaces. Therefore, as zeta potential parameter is elevated there is a tendency for cations to be transported in the direction of the cathode and entrain via dragging, electrolyte molecules creating an intensification in the electroosmotic flow (EOF). This produces the *weak deceleration* in *axial flow* in the lower half space with a compensatory *weak acceleration* in the upper half space. However, the zeta potential difference increment is not sufficiently strong to initiate any modifications in the transverse flow which remains essentially invariant across the

entire gap. It is also noteworthy that increased ionic strength of the electrolyte (desirable in efficient lubrication [18]) produces stronger double-layer compression and hence a decreased zeta potential, and a concomitant decrement in electro-osmotic body force. Therefore, while alterations may arise in the transverse flow with very high zeta potential differences, which may be explored in future studies, lower zeta potential is more appropriate for the current study.

Fig. 8 shows the influence of the *rotation parameter* Ω on the axial velocity $f'(\eta)$ and transverse velocity $g(\eta)$ profiles. The Coriolis body force is simulated in the term, *-S(Ωg′)* in the axial momentum Eqn. (18) and the term + *S(Ωf′)* in the transverse momentum Eqn. (18). The rotational effect is therefore generated by the cross-play of velocity components. Increment in rotational parameter, Ω, therefore accentuates the *-S(Ωg′) term (an inhibiting force)* which leads to a deceleration in the axial flow in the lower half space and partially encroaches into the upper half space zone. Further towards the upper plate, via momentum conservation, the axial flow is weakly accelerated. However the *+ S(Ωf′) is assistive and strongly enhanced transverse velocity across the entire gap with increment in rotation parameter (*Ω*).* For the case, Ω *= 0, rotational effects are negated* i. e. only axial momentum is considered, and the transverse velocity vanishes as observed in the figure. A noticeable sensitivity in the squeezing flow is present with strong rotational effect, and this may be exploited to achieve desired flow characteristics in dual disk lubrication systems. Even at high values of Ω, *flow reversal is never computed* as confirmed by the consistently positive values of both axial and transverse velocity.

Fig. 9, illustrates the influence of lower plate suction parameter on axial and transverse velocity components, $\left(f'(\eta)\&g(\eta)\right)$. The upper plate is solid. However lateral mass influx out of the gap is achieved via the lower disk boundary condition, $f(0) = \beta$, in Eqn. (21). As $\beta = \frac{2V_0}{aH}$ is increased, the intensity of fluid mass removal via the lower plate is increased. This causes the ionic liquid to adhere more strongly to the plate and thickens the boundary layer. A strong axial flow deceleration is computed with increasing β, and this is maintained across the gap due to the damping in the flow. A peak axial velocity is computed for the solid lower plate case (β =0) near the gap centreline. However, this peak is displaced to the lower plate with increasing suction. A weaker suppression in transverse velocity is induced with increasing suction. However, the peak velocity is always observed at the centre of the gap irrespective of whether the lower plate is *impervious* (β=0) or *strong suction* is present (β=0.5). The transverse velocity profiles are

always symmetric about the gap centreline (η=0.5). Effectively an excellent facility for regulating the flow characteristics is available via the inclusion of a lower plate.

Figs. 10–14 depict the effects of the key parameters on the pressure gradient, $/d\eta$. The influence of both positive and negative squeezing parameter (S) i. e. separating ($S > 0$) and approaching ($S < 0$) plates, on the pressure gradient distribution $dp/d\eta$ is seen in **Fig. 10**. With ($S < 0$) since the plates approach each other, squeezing is generated, and a negative pressure gradient is produced across the gap. This decays from the lower plate to the upper plate in a linear fashion. However, with separating ($S > 0$) plates, greater space is afforded to the lubricant and a positive pressure distribution is obtained which grows in a monotonic profile from the lower disk to the upper disk. For the case of stationary plates ($S = 0$) at a fixed distance apart, *no pressure gradient* is induced, as expected, since there is no modification in the stresses applied to the intercalated fluid.

The influence of magnetic parameter M on the pressure gradient $dp/d\eta$ is displayed in **Fig. 11**. As can be observed in the image, an unfavourable pressure gradient grows in the neighbourhoods of both plates as the Lorentz force increases. However, this adverse pressure gradient reduces in the central gap zone channel as the Lorentz force diminishes i. e. with a decrement in Hartmann number. In the central zone, strong magnetic field ($M = 2$) still sustains a favourable (*positive*) pressure gradient, which is critical for load carrying capacity of the system. For the electrically non-conducting case ($M = 0$), minimum pressure gradient arises near the lower and upper plates whereas a maximum value is observed at the centre of the gap. However, pressure gradient profiles are skewed towards the upper plate and not symmetrical about the centreline location, irrespective of the value of Hartmann number. Maximum pressure gradient is computed at the upper disk for the strongest magnetic field case ($M = 2$).

Fig. 12 shows the effects of the rotation parameter Ω on the pressure gradient $dp/d\eta$. It is clear from this that a considerable amount of rotation produces a positive pressure gradient at the lower plate but a much higher value of pressure gradient arises at the upper plate. Several trends in the pressure gradient may be seen in the main flow regime. The pressure gradient in the lower half of the gap is adverse, the pressure gradient in the centre is reduced, and the pressure gradient in the upper half space is favourable, with increasing rotational body force effect. A much steeper gradient is computed for pressure gradient profiles in the upper half space than in the lower half space. In addition, it should be noted that an oscillatory topology is computed at the highest value of the rotation parameter $\Omega = 2$ indicating that with the most intense rotation (i. e. greatest

angular velocity, ω, as $\Omega = \frac{2\omega}{a}$) there is *flow instability* generated in the regime. Lower values ensure a more consistent response in pressure gradient implying that a judicious selection for rotational velocity is required in lubrication design. In Fig. 10 several values have also been highlighted at distinct locations in the gap - $\eta = 0.05, 0.5 \& 0.85$.

Figs. 13 and 14 show the collective effects of the electroosmosis parameter m and the electric field parameter Ue on the pressure gradient, $dp/d\eta$. It is apparent that as the electroosmosis parameter m is increased and for *positive* electric field parameter Ue (i.e. reversed axial electrical field direction), the pressure gradient is elevated at the lower and upper plates whereas it is diminished in the core zone. Asymmetry of the pressure gradient profiles is also observed again about the centre line of the gap. The electro-osmotic parameters therefore modify the pressure gradient across the gap but maintain positive values at every location. This ensures an effective load carrying capacity in the lubrication design. Negative pressure gradient never arises even at relatively strong values of axial electrical field as simulated via the $U_{hs} = -\frac{2k_B T_H \varepsilon_{ef} E_x}{\mu z e}$ and electrical double layer (EDL) thickness as analyzed via the parameter, $m^2 = K^2 H^2 (1 - at)$ in Eqn. (18). Pressure distribution in the gap is therefore effectively manipulated with the electro-osmotic effects.

Figs. 15–18, present the influence of the electric field parameter Ue, electroosmosis parameter m, Hartmann number M and rotation parameter Ω on the upper disk skin friction coefficient $f''(1)$ versus squeezing parameter S. The upper wall skin friction coefficient exhibits a linear decay as the squeezing parameter changes from negative $S < 0$ (approaching plates i. e. squeezing) to positive $S > 0$ (separating plates) conditions. Skin friction is substantially depressed with *positive* electric field parameter Ue whereas it is enhanced with negative *positive* electric field parameter Ue (Fig. 15). A strong decrement in skin friction also accompanies an increase in electroosmosis parameter m (Fig. 16) and Hartmann magnetic number M (Fig. 17) indicating that strong axial flow deceleration is induced at the upper disk of the lubrication system with a reduction in EDL thickness and stronger magnetic field intensity (greater Lorentz magnetic forces). Thus, the upper plate experiences slower shearing and lower skin friction is computed. A distributed electromagnetic ionic lubrication system can therefore benefit from the simultaneous application of electrical and magnetic fields, when ionic magnetized working lubricants are deployed.

Fig. 18 shows that with increasing rotation parameter, Ω, the upper plate skin friction is reduced for higher values of *negative S and positive S*. However, at intermediate values of S (-0.2< S< 0.2) the skin friction is not tangibly altered. In other words, with weak departure (separating plates) or weak squeezing (approaching plates) the Coriolis body force exerts no significant effect on the upper disk skin friction. Maximum magnitude of skin friction is produced for the non-rotating scenario ($\Omega = 0$) when S = 01 (strong squeezing). However, the minimal magnitude of skin friction is produced for strongest rotation (($\Omega = 4$), for the strong plate separating case (S = 1). Axial flow acceleration is therefore maximized for the former case and minimized for the latter at the upper disk. A significant alteration in viscous drag at the upper disk is therefore achievable with the appropriate combination of squeezing and rotation parameters in the regime.

7. CONCLUSIONS

A theoretical study of the squeezing flow of a smart ionic magneto-tribological fluid with zeta potential effects, intercalated between two parallel plates rotating in unison, under the simultaneous application of electric and magnetic fields, has been presented. The lower disk permits lateral mass flux (suction or injection). The formulation features a more robust approach to the traditional Poisson-Boltzmann equation model. A similarity transformation is used to transform the governing equations into ordinary differential equations, which are then numerically solved with appropriate boundary conditions at the disks using MATLAB software (bvp4c solver). Via graphical visualization of velocity profiles, pressure gradients and the upper disk coefficient of skin friction, several key characteristics of squeezing flow are analysed. The computations show that:

(i) In the lower half space of the gap, increasing the electric field parameter Ue and electroosmosis parameter m (inverse EDL parameter) induces a rise in axial and transverse velocities, whereas the converse behaviour is generated in the upper half space of the gap.

(ii) An increase in the rotation parameter Ω leads to a rise in axial velocity in the lower half space, with the opposite effect produced in the upper half space.

(iii) The pressure gradient is reduced in the gap core zone with elevation in Hartmann magnetic number M, electrical field parameter, Ue, electro-osmotic parameter m and rotation parameter, Ω.

(iv) The upper disk skin friction coefficient decays in a linear fashion as the squeezing parameter changes from negative $S < 0$ (approaching plates i. e. squeezing) to positive $S > 0$ (separating plates) conditions.

(v) Upper disk skin friction is markedly reduced with *positive* electric field parameter Ue whereas it is enhanced with negative *positive* electric field parameter Ue .

(vi) Upper disk skin friction is depleted with increment in electroosmosis parameter m and Hartmann magnetic number.

(vii) Pressure gradient profiles are asymmetric about the centre line of the gap and are skewed towards the upper disk.

(viii) Pressure gradient is enhanced at the lower and upper plates whereas it is diminished in the core zone with an increment in electroosmosis parameter m and for *positive* electric field parameter Ue (i. e. reversed axial electrical field direction).

(ix) An increase in rotational parameter, Ω, results in a strong transverse velocity enhancement *across the entire gap* from the lower disk to the upper disk.

(x) Increasing zeta potential parameter generates a *weak deceleration* in *axial flow* in the lower half space with a compensatory *weak acceleration* in the upper half space. However, the zeta potential difference increment has no tangible influence on the transverse velocity across the entire gap.

(xi) A strong axial flow deceleration is computed with increasing lower disk suction parameter, β, and this is sustained across the gap. A weaker decrement in transverse velocity is induced with increasing suction.

The present study has revealed some interesting insights into rotating EMHD (electromagnetohydrodynamic) squeezing flows of relevance to micro-tribological designs. However, attention has been confined to Newtonian fluid behaviour. Future studies may implement *non-Newtonian* models for ionic magnetic lubricants e.g. microstructural, viscoelastic etc. Furthermore, bio-inspired lubrication systems are also growing in popularity which feature biological doping of squeeze films with micro-organisms [58].

REFERENCES

1. Gibson A.G, Kotsikos G, Bland J.H. Toll S. Squeeze flow. In: Collyer A.A., Clegg D.W. (eds) *Rheological Measurement*. Springer, Dordrecht, Netherlands, 1998. PP.550-591.
2. Ishizawa S. The unsteady flow between two parallel discs with arbitrary varying gap width. *Bulletin of the Japan Society of Mechanical Engineers*. 1966; 9: 533–550.
3. Estellé P, Lanos C, Perrot A, Servais C. Slipping zone location in squeeze flow. *Rheol Acta* 2006; 45: 444-448.

4. Meeten GH. Effects of plate roughness in squeeze-flow rheometry. *J Non-Newtonian Fluid Mech.*, 2004;124:51-60.
5. Mahmood M, Asghar S, and Hossain M. Squeezed flow and heat transfer over a porous surface for viscous fluid, *International Journal of Heat and Mass Transfer*, 2007; 44(2): 165-173.
6. Hayat T, Khan M, Imtiaz M, and Alsaedi A. Squeezing flow past a Riga plate with chemical reaction and convective conditions, *Journal of Molecular Liquids*, 2017; 225: 569-576.
7. Bike S. G, Prieve D. C. Electrohydrodynamic lubrication with thin double layers. *J. Colloid Interf. Sci*., 1990; 136(1): 95–112.
8. Bruus H. *Theoretical Microfluidics*, Oxford Master Series in Condensed Matter Physics, Oxford University Press, Oxford, UK, 2008. PP.157-170.
9. Reuss F.F. Sur un nouvel effet de l'electricite galvanique, *Memoires de la Societe Imperiale des Naturalistes de Moscou.,* 1809; 2: 327–337.
10. C-H Hsu *et al*., Magneto-hydrodynamic squeeze film characteristics between circular discs including rotational inertial effects, *Proceedings of the Institution of Mechanical Engineers, Part J: Journal of Engineering Tribology*, 2008; 222 (2): 157-164.
11. Ravikumar R, Arul Freeda Vinodhini G, Prakash J. Heat transfer and slip effects on the MHD peristaltic flow of viscous fluid in a tapered microvessels: application of blood flow research, *International Journal of Engineering and Advanced Technology (IJEAT)*, 2019; 9(1): 5384-5390.
12. Prakash J, Balaji N, Siva E.P and Chanrasekaran A.D. Non-linear blood flow analysis on MHD peristaltic motion of a Williamson fluid in a micro channel, *AIP Conference Proceedings* 2112 24 June 2019 paper no. 20048, PP-1-11.
13. Govindarajan A and Vidhya M, Siva E. P, Prakash J. MHD peristaltic transport of a dusty couple stress fluid through a symmetric porous channel, *International Journal of Engineering & Technology*, 2018; 7 (4.10); 306-309.
14. Li W-L and Jin Z. Effects of electrokinetic slip flow on lubrication theory, *Proceedings of the Institution of Mechanical Engineers, Part J: Journal of Engineering Tribology*, 2008; 222: 109-120.
15. Phillips B. S, Zabinski J. S. Ionic liquid lubrication effects on ceramics in a water environment. *Tribol. Lett*., 2004; 17(3): 533–541.
16. Wong P. L, Huang P, Meng Y. The effects of the electric double layer on a very thin water lubricating film. *Tribol. Lett.*, 2003; 14(3): 197–203.

17. Talapatra S & Chakraborty S. Squeeze-flow electroosmotic pumping between charged parallel plates. *Intl J. Fluid Mech. Res.* 2009; 36: 460–472.
18. Zhao C, Zhang W, Dirk van den Ende, Mugele F. Electroviscous effects on the squeezing flow of thin electrolyte solution films, *Journal of Fluid Mechanics*, 2020; 888, A29: 1-38.
19. Mat Noor NA, Shafie S, Admon MA. Unsteady MHD squeezing flow of Jeffrey fluid in a porous medium with thermal radiation, heat generation/absorption and chemical reaction. *Physica Scripta*. 2020; 95(10): https://doi.org/10.1088/1402-4896/abb695.
20. Shah R. C and Patel D. B. Analysis and comparative study of ferrofluid lubricated circular porous squeeze film-bearings, *Proceedings of the Institution of Mechanical Engineers, Part J: Journal of Engineering Tribology*, 2017; 231: 1450-1463.
21. Domairry G, Aziz A. Approximate analysis of MHD Squeeze flow between two parallel disks with suction or injection by homotopy perturbation method. *Mathematical Problems in Engineering*, 2009; Article ID 603916: 1-19.
22. Adesanya S. O, Ogunseye H. A, and Jangili S. Unsteady squeezing flow of a radiative Eyring-Powell fluid channel flow with chemical reactions, *International Journal of Thermal Sciences*, 2018; 125: 440-447.
23. Umavathi J.C, Patil S.L, Mahanthesh B and Anwar Bég O. Unsteady squeezing flow of magnetized nano-lubricant between parallel disks with Robin boundary condition, *Proc. IMechE J. Nanomaterials, Nanoengineering and Nanosystems* 2021; 135(3-4): 67-81.
24. Prajapati BL. Magnetic-fluid-based porous squeeze films, *J. Magn. Magn. Mater.* 1995; 149: 97–100.
25. Khan, Umar, Naveed Ahmed, Zaidi Z. A, Mir Asadullah, and Syed Tauseef Mohyud-Din. MHD squeezing flow between two infinite plates. *Ain Shams Engineering Journal*, 2014; 5 (1): 187-192.
26. Herr, A. E, Molho J. I, Santiago J. G, Mungal M. G, Kenny T. W, and Garguilo M. G. Electroosmotic capillary flow with nonuniform zeta potential. *Analytical Chemistry*, 2000; 72 (5): 1053-1057.
27. Yang R-J, L-M. Fu, and Y-C. Lin. Electroosmotic flow in microchannels. *Journal of Colloid and Interface Science*, 2001; 239(1): 98-105.
28. Kang, Yuejun, Chun Yang, and Xiaoyang Huang. Electroosmotic flow in a capillary annulus with high zeta potentials. *Journal of Colloid and Interface Science*, 2002; 253(2): 285-294.

29. Haywood, Daniel G, Zachary D. Harms and Stephen C. Jacobson. Electroosmotic flow in nanofluidic channels. *Analytical Chemistry*, 2014; 86(22): 11174-11180.
30. Helmholtz H. Uber den Einflus der elektrischen Grenzschichten bei galvanischer Spannung und der durch Wasserstromung erzeugten Potentialdifferenz, 1879; 7: 337.
31. Von Smoluchowski M. Versuch einer mathematischen Theorie der Koagulationskinetic kolloid Losungen, *Z. Phys. Chem*. 1917; 92: 129–135.
32. Burgreen D, Nakache F.R. Electrokinetic flow in ultrafine capillary slits, *J. Phys. Chem*. 1964; 68: 1084–1091.
33. Prakash J, Tripathi D. Study of EDL phenomenon in peristaltic pumping of a Phan-Thien-Tanner fluid through asymmetric channel, *Korea-Australia Rheology Journal*, 2020; l. 32 (4): 271-285.
34. Bharathi V, Vijayaragavan R, Prakash J. A study of electro-osmotic and magnetohybrid nanoliquid flow via radiative heat transfer past an exponentially accelerated plate, *Heat Transfer*, 2021; 50 (5): 4937-4960.
35. Prakash J, Yadav A, Tripathi D, Tiwari AK. Computer modelling of peristalsis-driven intrauterine fluid flow in the presence of electromagnetohydrodynamics, *The European Physical Journal Plus*, 2019; 134 (2): Article ID 81: 1-20.
36. Rajaram V, Varadharaj B, Prakash J. A study of electro-osmotic and magnetohybrid nanoliquid flow via radiative heat transfer past an exponentially accelerated plate, *Heat Transfer*, 2021; 50 (5): 4937-4960.
37. Gabai Ran, Ilssar Dotan, Shaham Ran, *et al.* A rotational traveling wave-based levitation device—modelling, design, and control. *Sens Actuat A*., 2017; 255: 34–45.
38. Turkyilmazoglu, M. Unsteady flow over a decelerating rotating sphere. *Physics of Fluids* 30, no. 3 (2018): 033601.
39. Turkyilmazoglu, M. Direct contact melting due to a permeable rotating disk. *Physics of Fluids* 31, no. 2 (2019): 023603.
40. Turkyilmazoglu, Mustafa. MHD fluid flow and heat transfer due to a stretching rotating disk. *International Journal of Thermal Sciences* 51 (2012): 195-201.
41. Turkyilmazoglu, Mustafa. Three dimensional MHD stagnation flow due to a stretchable rotating disk. *International Journal of Heat and Mass Transfer* 55, no. 23-24 (2012): 6959-6965.
42. Munawar S, Mehmood A, Ali A. Three-dimensional squeezing flow in a rotating channel of lower stretching porous wall, *Computers and Mathematics with Applications*, 2012; 64: 1575–1586.

43. Arain M. B, Bhatti M. M, Zeeshan A, Alzahrani F and Anwar Bég O. Radiative bioconvection nanofluid squeezing flow between rotating circular plates: semi-numerical study with the DTM-Padé approach, *Modern Physics Letters B.* 2021; Article ID 2141020:1-10.
44. Zueco J and Anwar Bég O. Network numerical analysis of hydromagnetic squeeze film flow dynamics between two parallel rotating disks with induced magnetic field effects, *Tribology International*, 2010; 43: 532-543.
45. Anwar Bég O, Tripathi D, Sochi T and Gupta PK. Adomian decomposition method (ADM) simulation of magneto-biotribological squeeze film with magnetic induction effects, *J. Mechanics Medicine Biology,* 2015; 15: 1550072.1-1550072.23.
46. Khatun S, Islam M.M, Mollah M.T, Poddar S, Ala M.M. EMHD radiating fluid flow along a vertical Riga plate with suction in a rotating system, *SN Applied Sciences* 2021; 3: Article number: 452, 1-15.
47. Riasat,M. Ramzan S, Kadry S, Chu Y.M. Significance of magnetic Reynolds number in a three-dimensional squeezing Darcy–Forchheimer hydromagnetic nanofluid thin-film flow between two rotating disks, *Scientific Reports* 2020; 10: Article number: 17208, 1-20.
48. Siva T, Jangili S, Kumbhakar B. Heat transfer analysis of MHD and electroosmotic flow of non-Newtonian fluid in a rotating microfluidic channel: an exact solution, *Applied Mathematics and Mechanics*, 2021; 42: 1047–1062.
49. Abhimanyu P, Kaushik P, Mondal P. K, Chakraborty S. Transiences in rotational electro-hydrodynamics microflows of a viscoelastic fluid under electrical double layer phenomena. *Journal of Non-Newtonian Fluid Mechanics*, 2016; 231, 56–67.
50. Li, S. X., Jian, Y. J., Xie, Z. Y., Liu, Q. S., And Li, F. Q. Rotating electro-osmotic flow of third grade fluids between two microparallel plates. *Colloids and Surfaces A: Physicochemical and Engineering Aspects*, 2015; 470: 240–247.
51. QI, C. and NG, C. O. Rotating electroosmotic flow of an Eyring fluid. *Acta Mechanica Sinica*, 2017; 33: 295–315.
52. Siva T, Kumbhakar B, Jangili S and Mondal P. K. Unsteady electro-osmotic flow of couple stress fluid in a rotating microchannel: an analytical solution. *Physics of Fluids*, 2020; 32: Article number: 102013, 1-12.
53. Umavathi J.C and Anwar Bég O. Computation of Von Karman thermo-solutal swirling flow of a nanofluid over a rotating disk to a non-Darcian porous medium with

hydrodynamic/thermal slip, *J. Thermal Analysis and Calorimetry*, 2021; https://doi.org/10.1007/s10973 -021-11126-1 (16 pages).

54. Wang C.Y. The squeezing of fluid between two plates, *ASME J. Appl. Mech*. 1976; 43 (4): 579–583.
55. Neelakanta P.S. *Handbook of Electromagnetic Materials*, CRC Press, Florida, USA, 1995.
56. Cramer K.C and Pai SI. *Magnetofluid Dynamics for Engineers and Applied Physicists*, MacGraw-Hill, New York, USA (1973).
57. Jihoon Mun and Haeun Sim (Editors), *Handbook of Ionic Liquids: Properties, Applications and Hazards*, Nova Science, New York, USA, 2012.
58. Shamshuddin M. Mishra S.R, Ali Kadir and Anwar Bég O. Unsteady chemo-tribological squeezing flow of magnetized bioconvection lubricants: *numerical study, J. Nanofluids*, 2019; 8 (2): 407-419.
59. J.H. He, Application of homotopy perturbation method to nonlinear wave equations, *Chaos Solitons & Fractals*, 26 (2005): 695-700.
60. J.H. He, Homotopy perturbation method for bifurcation of nonlinear problems, *International Journal of Nonlinear Science and Numerical Simulation*, 6 (2005): 207-208.